Coordination Chemistry Reviews 255 (2011) 2704–2726

Contents lists available at ScienceDirect

Coordination Chemistry Reviews

journal homepage: www.elsevier.com/locate/ccr

Review

A computational approach to the electronic and optical properties of Ru(II) and Ir(III) polypyridyl complexes: Applications to DSC, OLED and NLO

Simona Fantacci*, Filippo De Angelis

Istituto CNR di Scienze e Tecnologie Molecolari (ISTM-CNR), c/o Dipartimento di Chimica, Università di Perugia, Via elce di Sotto 8, I-06213, Perugia, Italy

Contents

ARTICLE INFO

Article history:
Received 17 November 2010
Accepted 8 March 2011
Available online 16 March 2011

Keywords:
Ru(II)
Ir(III)-polypiridyl complexes
Dye-sensitized solar cells (DSCs)
Organic light emitting diodes (OLEDs)
Non-linear optical (NLO) response

ABSTRACT

Ruthenium(II) and Iridium(III) polypyridyl complexes have been intensively investigated due to their use in energy conversion and light-emitting devices and materials for non-linear optics. Quantum mechanical computer simulations of molecules and materials have become increasingly popular in the scientific community. Along with experimental investigations, such computational analyses can provide complementary information on the electronic and optical properties of transition metal compounds of interest for optoelectronic applications. Here, we provide a unified review of recent work carried out on computational investigations of a large series of Ruthenium(II) and Iridium(III) polypyridyl complexes, discussing the relations between their electronic structure and optical properties and their device functioning. Our results, obtained for vastly different systems, allow us to trace some general conclusions concerning the modeling of these transition metal complexes, casting the bases for the computational design and screening, even before their synthesis, of new and more efficient transition metal complexes for photonics applications.

1. Introduction

Scientific and technological research and development is the engine of the "green revolution" which is driving the world economy towards a sustainable growth on a grand scale. Renewable energy sources and low cost devices which use high technology and smart materials for specific functions, are topics of great relevance for academic and industrial research. A global challenge is to capture and utilize solar energy for a sustainable development and to use the produced energy for low-cost, low-consumption lighting solutions. In this respect dye-sensitized solar cells (DSCs) [1–6] and organic light-emitting diodes (OLEDs) [7–10] represent valuable examples of both technologies, which can also be integrated into a unique photonic device. Moreover efficient non-linear optical chromophores can be integrated into bulk materials employed in photonic and electrooptical devices, telecommunications, and opti-

* Corresponding author. Tel.: +39 075 585 5522; fax: +39 075 585 5606.
E-mail address: simona@thch.unipg.it (S. Fantacci).

0010-8545/$ – see front matter © 2011 Elsevier B.V. All rights reserved.
doi:10.1016/j.ccr.2011.03.008

cal data storage and processing [11], further expanding the aim and scope of photonic devices.

In molecular and material science, modeling and computer simulation have gained a central role thanks to the exponential growth of computing power delivered by modern computers paralleled by similarly significant advances in theoretical methods and algorithms. Therefore, molecular modeling is currently employed for (i) understanding the properties of materials at the atomistic and molecular level; (ii) identifying and rationalizing the fundamental chemical processes which mimic complex environments such as surfaces and heterointerfaces; (iii) guiding the synthesis and production of new materials via molecular design; (iv) designing and optimizing nanosystems for a variety of applications ranging from electronics to energy conversion and storage to the development of materials with specific target properties. Nowadays high-performance computers permit the theoretical study of systems of large dimensions and increasing complexity with unprecedented accuracy.

A major difficulty in the theoretical and computational simulation of transition metal complexes and nano-structured materials resides is the inherent complexity of the systems under investigation. The complex interatomic interactions underlying these systems call for the use of accurate computational techniques, while the large dimensions of these systems substantially limit the accuracy of the computational tools which can be employed. Even computational tools showing a reasonable compromise between their accuracy and computational overhead, still have to tackle the inherent complexity of systems composed by several hundred (thousand) atoms, which usually show a large number of relevant geometrical configurations. The situation is even more severe if one considers properties related to excited states, such as those we are dealing with in DSCs, OLEDs and materials for non linear optics (NLO).

To solve this very challenging issue, we have over time set up an integrated computational strategy based on a combination of different codes and techniques rooted on density functional theory (DFT). The accuracy reached by current exchange-correlation (XC) functionals, especially hybrid ones, such as the renowned B3LYP [12], coupled to the reasonable scaling of the computational cost with the systems dimensions, the increasing computer power of off-the-shelf PCs and the availability of general-purpose quantum-chemistry (ADF [13], Gaussian 03 [14], Dalton [15], and Turbomole [16], or solid state physics (QuantumEspresso [17], VASP [18], and Crystal [19]) packages has led to the routine application of DFT to systems of medium to large dimensions. Our computational toolbox is centered on the computational efficiency of the Car-Parrinello (CP) method [20,21], which allows us to investigate the dynamics of chemical reactions [22], to include the effect of thermal motion on the investigated properties [23,24] and to optimize the geometry of extended systems characterized by several local minima of the potential energy surface [25,26]. The results of CP simulations are then plugged into quantum chemistry packages to calculate the properties of interest [25,26]. In doing so, inclusion of solvation effects is mandatory to provide a direct connection of the calculated properties with the corresponding experimental quantities [27]. While explicit inclusion of solvent molecules has been limited to small to medium solutes [23,28], continuum solvation models [29,30], in which the solvent is treated as a structureless dielectric medium and the solvent is confined within a cavity defined by the molecular geometry, can be effectively employed to reduce the computational overhead. Typical implementations of continuum solvation models available in commercial program packages are the Polarizable Continuum Model (PCM) [31] and the COnductor-like Screening MOdel (COSMO) [32].

The time-dependent extension of DFT (TDDFT) [33] has become the method of choice to deal with excited state properties of medium to large systems due to its accuracy coupled to its reasonable scaling with the systems dimensions [34], even though some problems of current XC functionals have been highlighted for long-range charge-transfer excitations [35]. Nevertheless, TDDFT is currently successfully applied to the study of systems containing transition metal centers [36]. Considering the ground state geometry, TDDFT can thus effectively simulate absorption spectra. Non-equilibrium solvation models allow one to include the solvent response due to the excitation process [37]. TDDFT also allows the calculation of excited state geometries, due to recent implementations [38], thus opening the way to calculations of emission spectra and excited state dynamics. Efficient procedures for calculations of dense spectra have also been recently reported [39]. In the case of transition metal complexes the lowest excited states are generally of triplet character, so that an estimate of excited state geometries can be easily obtained by calculating the lowest SCF triplet state. Alternatively, TDDFT can be used also to calculate excited state geometries, following the work of Ahlrichs and coworkers [40].

The inclusion of relativistic effects into the computational toolbox becomes crucial for ground and excited state properties when heavy metals are present, as is the case for Ir(III) complexes. Relativistic effects are therefore included by both monoelectronic approximations, mainly useful for qualitative purposes, and by a higher level approaches based on the two/four components solution of the Dirac–Kohn–Sham equations [41].

Explicit calculation of the hyperpolarizability tensor can be performed by TDDFT, finite field and coupled-perturbed approaches, while application of the two-level model based on TDDFT excited state dipoles, transition dipole moments and transition energies allows us to qualitatively gauge the role of the underlying electronic excitations in determining the overall NLO response [42–44].

In the following we review the main results obtained in the simulation of dyes and their interactions with semiconductors in DSCs, the investigation of Ir(III) complexes as OLED emitters and the application of the latter as NLO-phores. The link between these systems is on the one hand the presence of a d^6 electron configuration of the related transition metal complexes and on the other hand their unique photophysical and photochemical properties which require a commonly accurate characterization of their excited states.

In the DSCs field, the ultimate goal is the computational modeling of combined dye/semiconductor heterointerfaces, investigating the dye adsorption mode onto TiO_2, the dye/TiO_2 energy levels alignment and electronic coupling, the nature and localization of the excited states at the dye/semiconductor interface, thus effectively relating the molecular features to the device efficiency parameters [27,45–54]. Moreover, prediction of the electronic and optical properties of Ru(II) dyes and Ir(III) emitters would allow the design and screening of new complexes [55–60], thus significantly reducing the synthetic and characterization effort. As a general trend, while calculations were able to quantitatively reproduce the spectroscopic properties of the investigated compounds, computational investigations of NLO-phores were only qualitatively in agreement with experimental hyperpolarizability trends [42–44]. Quantitative reproduction of NLO properties is indeed a difficult task and the accuracy of DFT/TDDFT approaches for such quantities is still a matter of debate.

2. Ru(II)-polypiridyl complexes for dye sensitized solar cells

DSCs represent a particularly promising approach to the direct conversion of light into electrical energy at low cost and with high

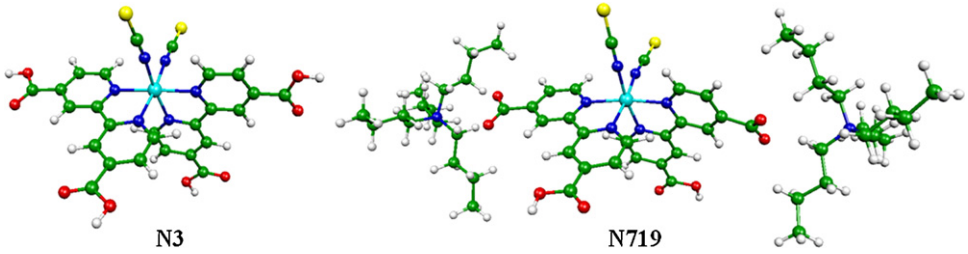

Fig. 1. Geometrical structures of N3 (left) and of the N719 complex (right).

efficiency [1–6]. In DSC devices, a dye sensitizer absorbs the solar radiation and transfers the photoexcited electron to a wide band-gap semiconductor electrode consisting of a mesoporous oxide layer composed of nanometer-sized particles, usually TiO_2, while the concomitant hole is transferred to a redox electrolyte [61], typically iodide/triiodide in solution or a hole-transporting material in the solid state. Various polypyridyl Ru(II) complexes are primarily employed as dye sensitizers [62]: the remarkable performance of the tetraprotonated [*cis*-(dithiocyanato)-Ru-*bis*(2,2′-bipyridine-4,4′-dicarboxylate)] complex (N3) and its doubly protonated analogue (N719), see Fig. 1, for which solar to electric power efficiencies exceeding 11% have been reported [45], had a central role in significantly advancing the DSCs technology [63]. Fully organic sensitizers have also been developed because of their increased molar extinction coefficient, spectroscopic tunability and reduced environmental impact compared to Ru(II)-dyes [52–54,64]. These dyes, however, have delivered reduced performance compared to the most efficient Ru(II) dyes. Although a substantial impulse to DSCs industrialization has recently emerged, for further progress higher photovoltaic conversion efficiencies need to be achieved. In this respect, there is a tremendous impetus in the design of new and more efficient sensitizers, and molecular engineering together with advanced quantum chemical calculations have in some cases been successfully employed [27,45–51].

In this section we report some of the most significant results obtained from the modeling of Ru(II)-dye sensitizers with direct application in DSCs. After a few initial studies, in the last 2–3 years there has been a significant amount of literature on this subject. We therefore retain only the earliest and/or more original contributions, highlighting the main information of relevance to DSCs and the related main methodological advances.

Due to the success of the N3 and N719 sensitizers (Fig. 1), most of theoretical/computational investigations have been initially devoted to this complex. Before we analyze such results, we briefly mention the pioneering work by Daul et al. on the related $[Ru(bpy)_3]^{2+}$ complex [65], for which the authors were able to describe the complex electronic structure and to assign its electronic transitions to metal to ligand charge transfer (MLCT) excitations, in agreement with the accepted experimental assignment [66].

2.1. The N3 dye: electronic structure and absorption spectra

To the best of our knowledge, the first theoretical investigation performed on N3 dates back to the work by Rensmo et al. [67]. In their joint semi-empirical theoretical and photoelectron spectroscopy study, these authors have investigated the electronic structure of the N3 complex in the gas-phase; by using a model geometry, they analyzed the energy and character of the N3 molecular orbitals in relation to the density of states obtained experimentally. In contrast to $[Ru(bpy)_3]^{2+}$, the HOMOs of N3 are an admixture of Ru-t_{2g} states with sulfur lone pairs and π orbitals of the thiocyanate ligands. The LUMOs were assigned to π^* orbitals of the functionalized bipyridine ligands, extending across the terminal carboxylic groups. The observed presence of thiocyanate character in the N3 HOMOs has important consequences for the regeneration of the oxidized dye, stabilizing the ensuing charge hole and allowing fast regeneration by iodide [68].

A few DFT/TDDFT papers on the N3 and related complexes appeared later, while a semiempirical ZINDO investigation on the $[Ru(4,4'\text{-COOH-}2,2'\text{-bpy})_2(Cl)_2]$ complex was reported earlier by Nazeeruddin et al. [69] Monat et al. simulated the absorption spectrum of the tetra-deprotonated form of N3 dye in gas-phase by TDDFT [70]. The calculated and experimental spectra were in fair agreement, including an almost quantitative reproduction of the dye molar extinction coefficient. Guilemoles et al. [71] addressed the ground and excited-state properties of related $[M(bpy)_2L_2]$ complexes (M = Ru, Os, L = CN, SCN, bpy = 2,2′-bipyridine). In that study, both geometry optimizations and TDDFT excited state calculations were performed in vacuo and in water solution. For the $[Ru(bpy)_2(NCS)_2]$ complex a substantial solvation effect was found, with calculated data in good agreement with the experiment. We reported the first DFT/TDDFT investigation on the N3 complex including the effect of different solvents on the electronic structure and absorption spectra [27]. The optimized N3 geometry was in excellent agreement with experimental structural parameters. A comparison between the electronic structure of the complex, in terms of frontier molecular orbitals, calculated in vacuo and in solution is reported in Fig. 2, upper panel.

In agreement with Rensmo et al. [67] for N3 we found the HOMO/HOMO−2 to constitute a set of quasi degenerate orbitals of mixed Ru/NCS character. The HOMO−3, found 0.25 eV below the HOMO−2, is localized entirely on the thiocyanate ligands, while at lower energy another set of three quasi degenerate orbitals is found, corresponding to the bonding counterpart of the HOMO/HOMO−2. The six lowest LUMOs are the antibonding π^* orbitals of the bipyridine ligands, with sizable contributions from the carboxylic groups (lower panel of Fig. 2) [27]. Because in DSCs the acidic carboxylic units serve as anchoring groups to the TiO_2 semiconductor surface, such a contribution from the carboxylic groups to the π^* LUMOs, which represent the final states in MLCT transitions, (see below), was assigned to favor the electron injection process from the dye excited state to the semiconductor surface. Inclusion of solvation effects leads to a sizable change of both energies and composition of the molecular orbitals. In ethanol, the lowest LUMOs are significantly destabilized, by ca. 0.3–0.4 eV with respect to the corresponding values computed in vacuo, even though they maintain a similar composition in terms of bipyridine and carboxylic group contributions. The first set of HOMOs is stabilized by 0.3–0.4 eV with respect to the corresponding values computed in vacuo, and also shows a higher contribution of Ru orbitals. The presence of the solvent leads to an important increase of the HOMO–LUMO gap [27]. Strong solvation effects have been observed also for the calculated absorption spectra in ethanol and water solution, which are reported in the upper panel of Fig. 3.

The overall shape and band separations of the N3 spectrum are well reproduced upon inclusion of solvation effects, reflecting the major changes in the electronic structure observed in

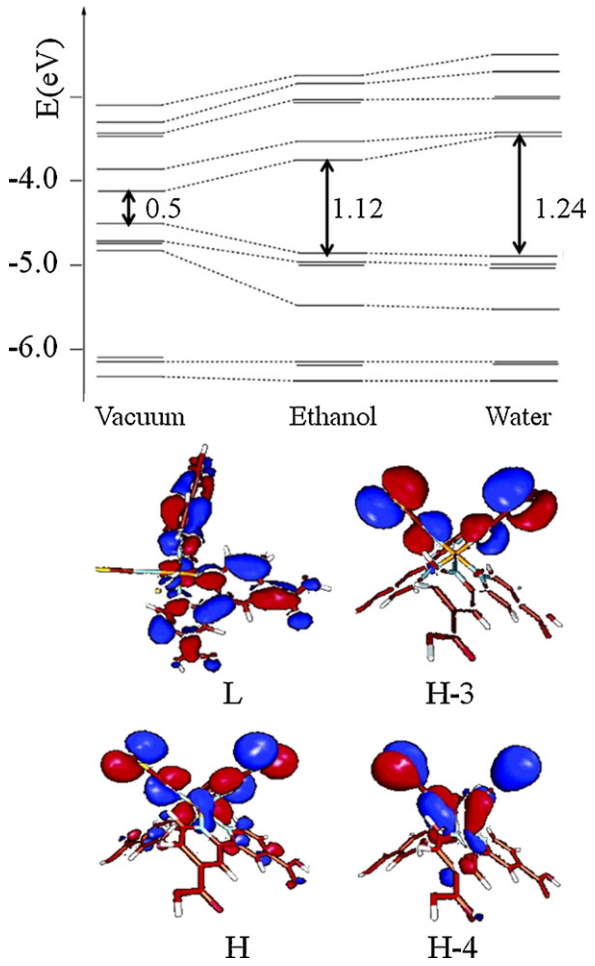

Fig. 2. Upper panel Molecular orbital energy for the protonated N3 species in vacuo and in ethanol and water solutions along with HOMO–LUMO gaps. Lower panel Isodensity plots of selected frontier molecular orbitals (L stands for LUMO, H for HOMO).
Adapted from Ref. [27].

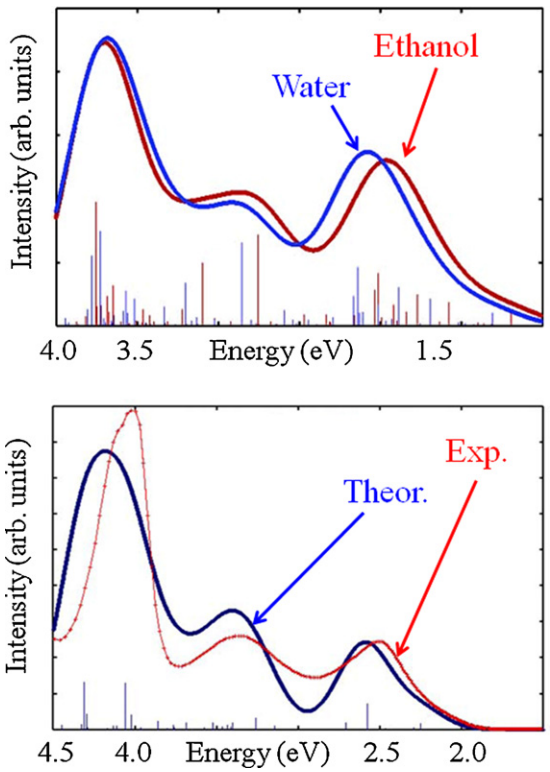

Fig. 3. Upper panel Calculated absorption spectra for the protonated N3 complex in ethanol and water solutions by the BPW91 xc functional. Lower panel Comparison between the experimental and calculated absorption spectra by the B3LYP xc functional for the tetra-deprotonated N3 complex in water solution.
Adapted from Refs. [27,47].

solution. The N3 calculated spectra are in good agreement with the experiment, apart from a quasi rigid red-shift of the entire spectra of ca. 0.3 eV. This inaccuracy is further lifted by using a hybrid xc functional, such as B3LYP; this can be seen in the lower panel of Fig. 3 where the comparison between the experimental and B3LYP/DZVP-calculated absorption spectra for the tetra-deprotonated N3 complex is reported [46,47]. The agreement between theory and experiment is excellent throughout an energy range of 4.5 eV. The two lowest energy bands were assigned to charge-transfer transitions to the bipyridine ligands, originating from hybrid orbitals made up of comparable metal and thiocyanate contributions. The third band, almost twice as intense as the first two bands, is assigned to intraligand π–π^* transitions. These results quantitatively reproduced the solvatochromic shifts exhibited by the N3 complex with increasing solvent polarity, which was related to a decreased dipole moment in the excited state with respect to the ground state. Compared to calculations for the tetra-deprotonated N3 complex in vacuo by Monat et al. [70], our TDDFT calculations in solution did not show any contribution from the deprotonated carboxylic groups to the HOMOs, since in solution the ensuing negative charge is effectively screened and these orbitals are found at lower energies. These early investigations recognized the importance of solvation effects on the electronic structure and optical properties of Ru(II)–polypyridyl dyes. Almost all the subsequent theoretical investigations therefore included solvation effects in the computational set-up, which are fundamental for a quantitative comparison with the experiments.

2.2. The N719 dye: influence of ligand protonation and counterions

We extensively investigated the effect of ligand protonation and the role of counterions on the N3 electronic structure. We focused on the N3 derived $(Bu_4N)_2[Ru(dcbpyH)_2(NCS)_2]$ complex, known as N719, by modeling for computational convenience the experimental bulky tetrabutylammonium counterions by sodium ions. We considered all the possible $[N3(xH - yNa)](x+y-4)$ complexes, where x is the number of protons, y is the number of Na^+ counterions, and the total charge of the molecule is $(x+y-4)$ [45]. For all of the investigated complexes, the energy pattern and character of the occupied orbitals is qualitatively similar to that of tetraprotonated N3. The bipyridine π^* LUMOs of the investigated complexes show a different localization depending on the protonation of the terminal carboxylic groups. For the N719 dye, Rensmo et al. by using photoelectron spectroscopy techniques found Ru contributions to the HOMOs in quantitative agreement to those computed by us [72], confirming their mixed Ru-t_{2g}/SCN-π nature [45]. For [N3(2H–2Na)](0), the model of N719, the LUMOs are essentially localized over the pyridine ligands bearing the protonated carboxylic groups, with higher lying orbitals localized over the pyridine ligands bearing the deprotonated carboxylic groups [45]. The stabilization of the π^* orbitals localized on the protonated ligand portions is a common feature of all the investigated Ru(II) dyes.

To provide a unified picture of ligand protonation and counterions effect on the dyes electronic structure, we lined up the frontier molecular levels of the different investigated species in Fig. 4,

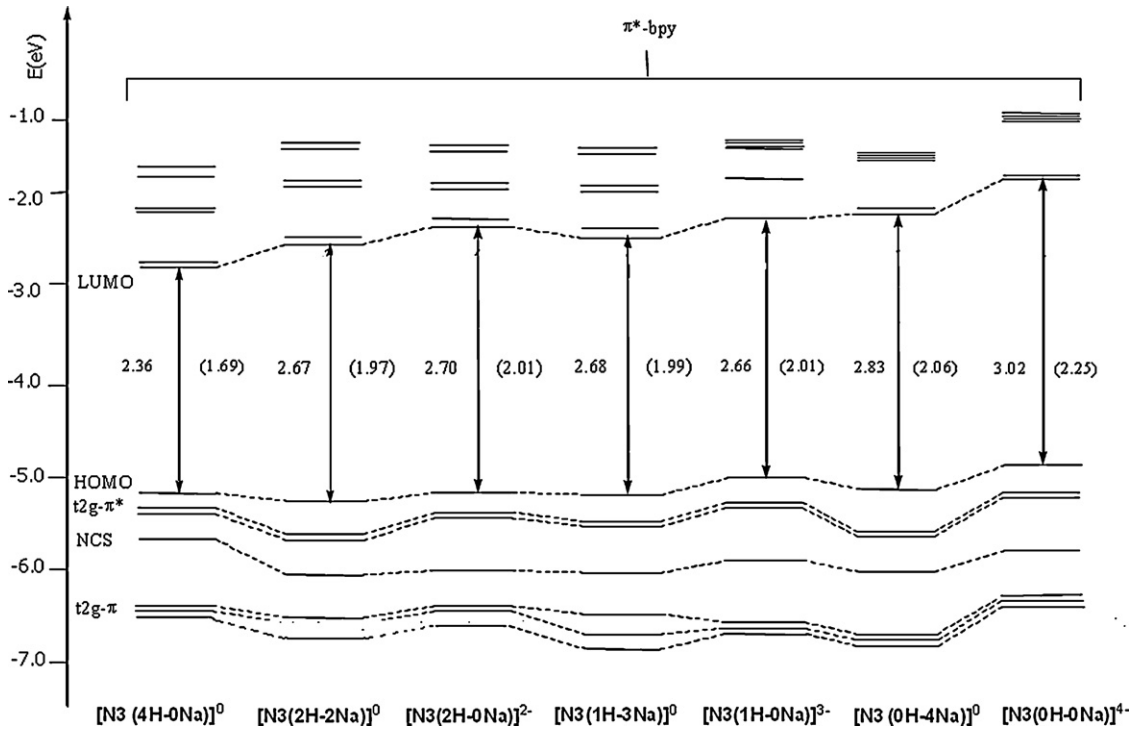

Fig. 4. Energy levels and lowest TDDFT singlet–singlet excitation energies (data in parentheses) calculated at the B3LYP/3-21G* level in water solution for the various dyes originated from the N3 complex. The bipyridine π bonding orbitals and the COO^- oxygen lone pairs are omitted for clarity.
Adapted from Ref. [45].

where we report the energy levels, the HOMO-LUMO gaps and the calculated lowest singlet–singlet TDDFT excitation energies. The [N3(4H–0Na)](0) complex shows the smallest HOMO–LUMO gap and the lowest singlet–singlet excitation energy among the considered dyes [45].

Moving to the neutral species, in [N3(2H–2Na)](0) the LUMO energy slightly raises with respect to N3, leading to an increased HOMO–LUMO gap and lowest excitation energies, see Fig. 4. For [N3(1H–3Na)](0) the occupied and unoccupied orbitals are only slightly higher in energy with respect to the di-protonated [N3(2H–2Na)](0) complex; the computed HOMO–LUMO gaps and first excitation energies are therefore similar for the two species. The LUMOs of the tetradeprotonated [N3(0H–4Na)](0) species lie at still higher energy. Removing the Na^+ counterions raises the energy of both the occupied and unoccupied orbitals by a similar amount, thus resulting in a HOMO–LUMO gap and first excitation energy similar to those of the corresponding complexes with counterions. On overall, in the case of the anionic complex, however, the shift of the unoccupied orbitals is considerably larger than that of the occupied ones, with a consequent increased HOMO–LUMO gap and lowest excitation energies. This shift of the unoccupied orbitals is related to the increased electron density on the deprotonated carboxylic groups which raises the energy of the bipyridine π* orbitals and results in an increase of the HOMO–LUMO gap and of the lowest excitation energy compared to the partially and fully protonated complexes [46]. This behavior is responsible of the relevant acidichromic effect observed in the N3 dye upon increasing the pH [46,73], which translates into a blue-shift of the main spectroscopic features increasing the pH from 1 to 9 [73].

To model these limiting pH situations, the absorption spectra of the N3 (completely protonated, pH 1.5) and its completely deprotonated analogous (pH 9) have been simulated and compared with the experimental spectra [46]. In Table 1, absorption maxima obtained at the B3LYP-DZVP level in water solution, are compared to experimental data and to results for the N3 species computed with the BPW91 functional. The spectroscopic shape of N3 and $N3^{4-}$ are rather similar, showing the presence of three bands, labeled I, II and III in order of increasing energy. The computed absorption maxima are in good agreement with the experimental data at pH 1.5 and 9 [73], both in terms of band separations and relative intensities of the main spectroscopic features. Most notably, our calculations are able to reproduce the observed blue-shift of the three main spectroscopic features with increasing pH, which is the signature of the acidichromic effect shown by the N3 complex.

2.3. Excited state oxidation potentials of Ru(II) dyes

We have established a computational approach which combines different DFT and TDDFT techniques to compute the excited state oxidation potential (ESOP) of Ru(II) sensitizers [74]. The dye ESOP value compared to the TiO_2 conduction band position, gives an estimate of the "driving force" for excited state electron injection, which, together with the electronic dye/semiconductor coupling, determines the rate of electron injection, and has therefore a central role in DSCs. The ESOP is generally expressed as the difference between the ground state oxidation potential (GSOP)

Table 1
Absorption maxima energies (eV), intensities ratios relative to band I (in parentheses), and band separations (ΔE(I–II) and ΔE(II–III), for the N3 and $N3^{4-}$ complexes in water compared with the experimental values from Ref. [73].

	I	II	III	ΔE(I–II)	ΔE(II–III)
Experimental N3	2.38 (1.0)	3.18 (1.0)	3.97 (–)	0.80	0.79
Theoretical[b]	2.41 (1.0)	3.02 (1.1)	3.96 (3.6)	0.61	0.94
Theoretical (BPW91/TZVP)[a]	2.08 (1.4)	2.92 (1.0)	3.69 (2.3)	0.84	0.77
Experimental $N3^{4-}$	2.48 (1.1)	3.33 (1.0)	4.03 (4.0)	0.85	0.70
Theoretical[b]	2.61 (1.0)	3.42 (1.5)	4.08 (3.8)	0.81	0.66

[a] Data from Ref. [27].
[b] Data from Ref. [46].

Table 2
HOMO (ε_{HOMO}) and LUMO (ε_{LUMO}) energies, ΔE^{v}_{ox}, ΔE^{v}_{red}, ΔG_{ox} (see text for definitions). HOMO-LUMO gap (Δ_{H-L}), lowest singlet-triplet ($S_0 \rightarrow T_1$) and singlet-singlet excitation energies ($S_0 \rightarrow S_1$), and excited states oxidation potentials obtained using the Koopman's theorem-based GSOP and $S_0 \rightarrow T_1$ / $S_0 \rightarrow S_1$ ($ESOP^{T}_{K}$ and $ESOP^{S}_{K}$, respectively) for N3 and N719 sensitizers. All values are reported in eV. Values are referred to the vacuum; in parenthesis values referred to the NHE potential.

Molecule	$-\varepsilon_{HOMO}$	$-\varepsilon_{LUMO}$	ΔE^{v}_{ox}	ΔG_{ox}	ΔE^{v}_{red}	Δ_{H-L}	$S_0 \rightarrow T_1$ ($S_0 \rightarrow S_1$)	$ESOP^{T}_{K}/ESOP^{S}_{K}$
N3	5.72 (1.28)	3.11 (−1.33)	5.78 (1.34)	5.50[a] (1.06)[a]	3.23 (−1.21)	2.61	1.76 1.93	3.96/3.79 (−0.48/−0.65)
N719	5.49 (1.05)	2.77 (−1.67)	–	–	–	2.72	1.87 2.00	3.63/3.49 (−0.81/−0.96)

Source: Data from Ref. [74].
[a] Values obtained considering vibrational contributions to the Gibbs free energies in vacuo calculated with the 3-21G* basis set.

and the lowest adiabatic excitation energy E_{0-0}. This basically represents a vertical approximation to the true ESOP, whose validity is generally believed to hold for Ru–polypyridine complexes, for which relatively low excited state reorganization energies are expected [75]. The GSOP can be rigorously calculated by computing the free energy difference between the neutral and oxidized species in solution. This requires one to include the translational, rotational and vibrational contribution to the total partition function. To avoid the geometry optimization of the oxidized species and the cumbersome calculation of vibrational frequencies, one approximation consists in estimating the vertical GSOP as the energy difference (in solution) between the neutral species at its optimized geometry and the oxidized species at the same geometry, neglecting the geometry relaxing of the oxidized system. An even less computationally demanding estimate of the vertical GSOP is to exploit Koopmans' theorem and thus to take the negative of the HOMO energy, $-\varepsilon_{HOMO}$, as an estimate of the vertical GSOP. We then simply approximate E_{0-0} with the lowest vertical excitation energy of the system at the ground state geometry, which can be efficiently and accurately calculated by TDDFT. With this approximation, however, the calculated ESOP values could be overestimated. For a closed-shell singlet ground state, both singlet–singlet and singlet–triplet excited states can be calculated. The calculated ESOP for the N3 and N719 dyes in water solution using the GSOP estimates outlined above are presented in Table 2. Our rigorous GSOP estimate for N3, ΔG_{ox}, yields to a value of 5.50 eV (1.06 eV) relative to the vacuum (NHE). The vertical approximation to the GSOP, ΔE^{v}_{ox}, differs by 0.28 eV from ΔG_{ox}, the energy difference corresponding to the dye reorganization energy in solution. The Koopmans' theorem estimate, 5.72 eV, is also in fair agreement with ΔE^{v}_{ox}. Clearly, both ΔE^{v}_{ox} and $-\varepsilon_{HOMO}$ represent upper bounds to ΔG_{ox} which is in excellent agreement with the 1.10 V (vs. NHE) oxidation potential reported for N3 in Ref. [75].

Using the approximate GSOP estimate, for N3 we calculate ESOP values of 3.96 and 3.79 (−0.48 and −0.65) eV relative to vacuum (NHE), considering the $S_0 \rightarrow T_1$ and $S_0 \rightarrow S_1$ lowest excitation energies, respectively. The analogous values, using the rigorous ΔG_{ox} are 3.74 and 3.57 (−0.70 and −0.87) eV relative to the vacuum (NHE), respectively [74].

For the N719 dye we limited our investigation to the vertical GSOP estimate based on the HOMO energy. The HOMO is destabilized in N719 compared with N3, due to the increased overall charge donation to the metal. The 0.23 eV energy up-shift is in excellent agreement with the 0.30 V decrease in oxidation potential measured experimentally [76]. Mainly as a result of the HOMO destabilization, the ESOP for N719 (−0.81/−0.95 eV versus NHE considering the $S_0 \rightarrow T_1$/$S_0 \rightarrow S_1$ transition) is substantially more negative compared with that one for N3 (−0.48/−0.65 versus NHE).

Experimentally, ESOP estimates of −0.65 and −0.98 V versus NHE have been reported for N3 and N719, respectively [45,75]. The measured ESOP difference of 0.33 V between N3 and N719 is well reproduced by our results which give a difference of 0.34 (0.31) eV for the $S_0 \rightarrow T_1$($S_0 \rightarrow S_1$) transitions. Remarkably, calculated absolute ESOP values are also in good agreement with the experiment, with values obtained using $S_0 \rightarrow S_1$ transitions reproducing almost exactly the experimental values (−0.65 and −0.96 eV versus −0.65 and −0.98 V, respectively). The excellent agreement between theory and experiment makes us confident that the established procedure can be rather safely employed for analogous Ru(II) dyes, providing a quick means to scrutinize the new dyes based on their GSOP and ESOP values.

2.4. Heteroleptic and cyclometalated Ru(II) dyes

In order to improve the DSCs efficiency, thousands of new dyes have been scrutinized and tested. Although delivering record efficiency, a major issue with N3 and N719 complexes is that they mainly absorb light in the green region of the visible spectrum, with molar extinction coefficients of the order of 14.000 $dm^3\,mol^{-1}\,cm^{-1}$, therefore losing out on a considerable amount of red and near-IR light. Starting from the N3 or N719 homoleptic sensitisers, a major research line has been devoted to synthesize heteroleptic sensitisers, in which one of the equivalent two bipyridine ligands of N3 or N719 is specifically functionalized to obtain increased DSCs' performances. Ligand engineering modifications aim at: (i) increasing the dye molar extinction coefficient, by extending the ligands conjugation and inserting heteroaromatic substituents, thus allowing for the use of thinner TiO_2 films; (ii) providing an improved dye stability, by inserting hydrophobic alkyl chains on the bipyridine ligands; and (iii) increasing the separation between the injected electrons onto TiO_2 and the oxidized dye, by introducing a supramolecular control of charge-transfer dynamics.

In this context, the [Ru(4,4′-dicarboxy-2,2′-bipyridine)(4,4′-tridecyl-2,2′-bipyridine4,4′-dicarboxy-2,2′-bipyridine)$(NCS)_2$], N621 and Z907 dyes, bearing the aliphatic chains in para to one of the ancillary bpy ligand, have shown increased stability in DSC devices [45,77]. The pH influence and the counterion effect on the electronic and optical properties of N621 have been investigated at the same level of theory used for N3. The main difference between N621 and N3 is due to the increased donation from the alkylated bipyridine, which locates the π^* orbitals localized on this ligand at higher energy. Representative examples of other heteroleptic dyes are: N945, where two 4,4′-di-(2-(3,6-dimethoxyphenyl)ethenyl groups are used to functionalize in para one bpy [49,78], C101 [79] and CYC-B1[80] (Z991), where antenna electron rich thiophene derivatives are used to increase the conjugation of the spectator bpy ligand, and SJW-E1 [81] and Ru-EDOT [50], which incorporates the 3,4-ethylenedioxythiophene (EDOT) substituents. Semi-empirical calculations (ZINDO/1) have been performed on C101 [79], CYC-B1 [80], (Z991) and SJW-E1 [81] complexes, while TDDFT calculations have been recently carried out on N945 [49] and Ru-EDOT [50]. We briefly mention the results obtained for the Ru-EDOT dye, Fig. 5, which is a representative example of HTSs.

B3LYP/DZVP calculations in ethanol solution revealed that the Ru-EDOT HOMO is a combination of Ru t_{2g} and SCN π orbitals, appreciably mixed with π-EDOT character. This is at variance

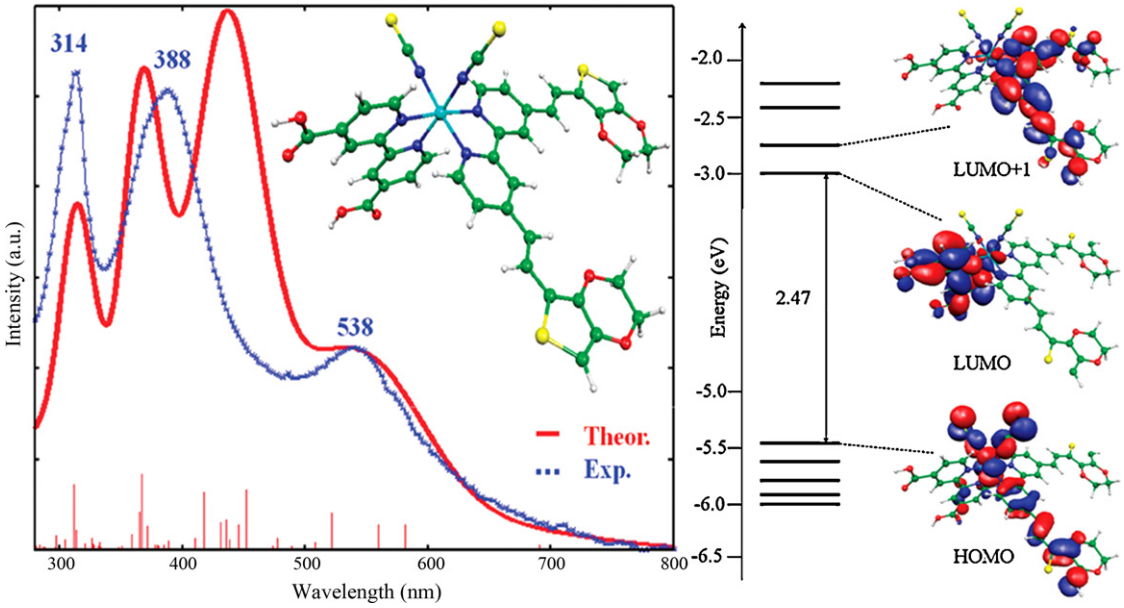

Fig. 5. Left: Structure of the Ru–EDOT complex and comparison between its experimental and calculated absorption spectra in ethanol solution. Right: Molecular orbital energies and isodensity plots of selected molecular orbitals for the Ru–EDOT complex.
Adapted from Ref. [50].

with the N621 complex, featuring an alkyl-substituted bipyridine ligand, for which a pure Ru–SCN HOMO, similar to that of N3, was found [45]. Such mixing is due to the conjugation with EDOT arms in the bipyridine ligand. Since the HOMOs are the starting orbitals for the low lying charge transfer transitions of Ru-EDOT, *vide infra*, the partial EDOT contribution to this orbital suggests that upon dye photo-oxidation, following electron injection into TiO_2, the positive charge is partially localized on the ligand, being stabilized by the electron-donation from the EDOT substituent. The LUMO is a π^* orbital localized on the protonated carboxy-bipyridine ligand, while the LUMO + 1, lying 0.26 eV above the LUMO, is a π^* orbital localized on the EDOT-substituted bipyridine. The TDDFT calculated absorption spectrum (Fig. 5) is in good agreement with the experimental spectrum for the low energy region, whereas some discrepancy in the intensity distribution is found at higher energies. The lowest excited state is originated from transitions to the LUMO, localized on the carboxylated bipyridine. The 538 nm absorption band is well reproduced by the theoretical approach (540 nm); this transition is localized on the EDOT-substituted bipyridine and shows higher intensity compares to the lower-lying excitation, due to the partial π–π^* character of this otherwise charge transfer excitation. The calculated absorption spectrum and the excited states order of Ru-EDOT are perfectly consistent with the high observed photovoltaic efficiencies. Indeed, excitation at about 540 nm will mainly lead to excited states localized onto the EDOT-substituted bipyridine. Since these heteroleptic sensitizers are adsorbed onto TiO_2 via the carboxy-bipyridine the presence of lower lying excited states residing on such ligands allows efficient energy transfer to this state, and subsequent efficient electron injection.

Alongside with the chemical modification of the bpy ligands, many attempts have been devoted to replace the thiocyanate ligands, which are believed to limit the temporal stability of DSC devices [82]. Recently, cyclometalated Ru(II) dyes have been reported, in which the two SCN groups are replaced with a substituted phenyl-pyridine (ppy) ligand [83,84]. The prototype YE05 dye, characterized by a ppy ligand bearing two fluorine substituents, has been demonstrated a promising candidate for its high stability and the broad range of visible light absorption compared with N719. DFT/TDDFT calculations revealed a substantial HOMO delocalization through the Ru-bound cyclometalated ligand, assisting regeneration of the oxidized dye and an extended light-harvesting capability compared with the standard N719 dye [83].

2.5. Trans-dithiocyanate Ru(II) complexes

Trans di-thiocyanate complexes have been investigated in order to increase the dye-sensitizer light-harvesting capability. The electronic structure of the trans N3 isomer (Fig. 6) is rather similar to that of the cis isomer discussed previously [27]. The most notable difference is a reduction of 0.18 eV in the HOMO–LUMO gap compared with the cis isomer. This value nicely compares with the experimental red shift of 0.17 eV observed for the first visible absorption band of the N3 complex upon cis to trans isomerization. Such an enhanced red response of the trans isomer makes trans-thiocyanate complexes attractive candidates as charge-transfer sensitizer in DSCs. In this context, a ruthenium trans-[Ru(L)$(NCS)_2$], with L = 4,4‴-di-tert-butyl-4′,4″-bis(carboxylic acid)-2,2′:6′,2″:6″,2‴-quaterpyridine complex, N886 (Fig. 6), was synthesized by Barolo et al. with the aim to enforce the stability of the trans thiocyanate coordination [48]. Both spectroscopic, electrochemical and theoretical calculations confirmed the enhanced red-response of this elegantly designed dye, which showed absorption bands of mixed Ru/SCN-to-quaterpyridine charge-transfer character extending from the near-IR to the UV regions.

A schematic orbital energy diagram of the doubly-protonated and doubly-deprotonated N886 complexes, calculated at the B3LYP/DZVP level in ethanol solution, is reported in the left panel of Fig. 7, along with isodensity plots of the frontier molecular orbitals.

The deprotonated complex differs from the protonated one for the HOMO–LUMO gap increase from 2.42 to 2.72 eV, due to a larger destabilization of the unoccupied with respect to the occupied orbitals. The TDDFT calculated absorption spectra of the protonated and deprotonated N886 complexes are shown in the right panel of Fig. 7. The main absorption features of the experimental spectrum are reproduced by theory, despite a red shift of the lowest-energy band in the visible region of the spectrum. This band, experimen-

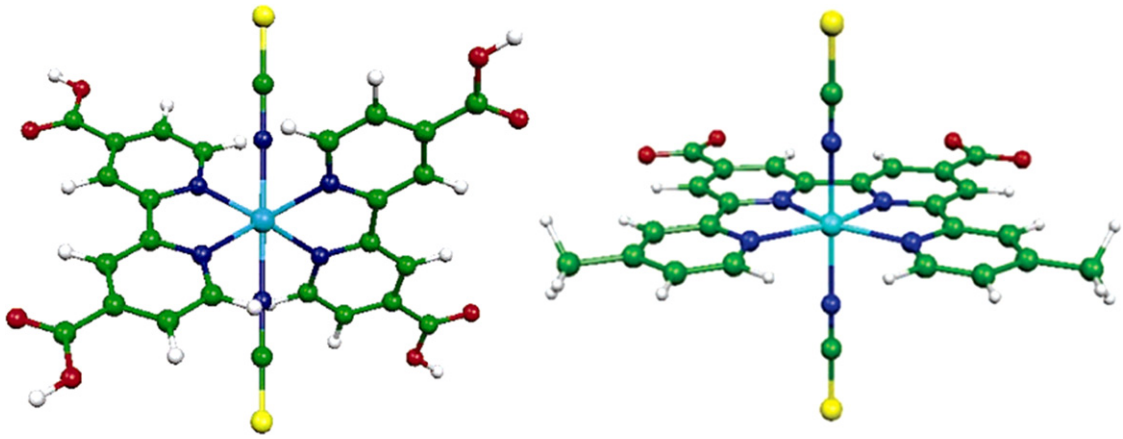

Fig. 6. Optimized molecular structures of the trans-N3 isomer (left) and of the N886 complex (right).

tally found at 637 nm, is calculated at 699 nm, i.e., only 0.17 eV red-shifted with respect to the experimental data, and appears to be composed of two transitions at 731 and 672 nm, which originated from the HOMO−1/HOMO (Ru-SCN) couple to the π^* LUMO. We therefore see that the lowest-energy band in the visible region originates from an excited state maximally localized on the ligand portion bearing the carboxylic groups. Despite this favorable localization of the excited states and the red-shifted absorption spectrum, this complex did not deliver the expected increase photovoltaic performances, probably because of dye aggregation onto the TiO_2 surface and unfavorable alignment of the dye excited states with the TiO_2 conduction band energy.

Another interesting example of trans complexes is represented by a heteroarylvinylene π-conjugated quaterpyridine Ru(II) sensitizer (N1044) [51]. This dye has an effective panchromatic absorption band, covering the entire visible spectrum up to the NIR region, and superior electrochemical characteristics with respect to previous representative Ru(II) bi- and quaterpyridine sensitizers. DFT calculations performed in solution at the B3LYP/DZVP level on both the protonated and deprotonated N1044 complexes revealed that also for this trans complex the HOMOs are a combination of Ru-t_{2g} and thiocyanate π orbitals with variable contributions. In line with previous investigation on N886 [48], the LUMO is partly localized over the protonated carboxylic groups. This situation should correspond closely to that of the complex adsorbed on TiO_2, whereby the positive Ti(IV) surface atoms partly saturate the carboxylate negative charge [70]. The TDDFT calculated absorption spectrum of the deprotonated complex is in good agreement with the measured spectrum both in terms of bands position and relative intensity (see Fig. 8 for a comparison between theory and experiment), suggesting that the deprotonated complex is the species effectively present in solution.

The broad low-lying transition recorded for the complex in solution at 615 nm is calculated by TDDFT at 640 nm, only 0.08 eV red-shifted compared with the experimental data. Such transition arises from a HOMO−1 to LUMO excitation (see the involved orbitals in the inset of Fig. 8). The broad absorption spectrum is originated from the superposition of this low-lying transition with a second group of MLCT features in the range 450–530 nm. The N1044 dye ESOP has been estimated as described above [74], providing values of 3.9 and 3.4 eV vs. vacuum for the protonated and deprotonated complex, respectively, i.e. −0.5 and −1.0 eV vs. NHE,

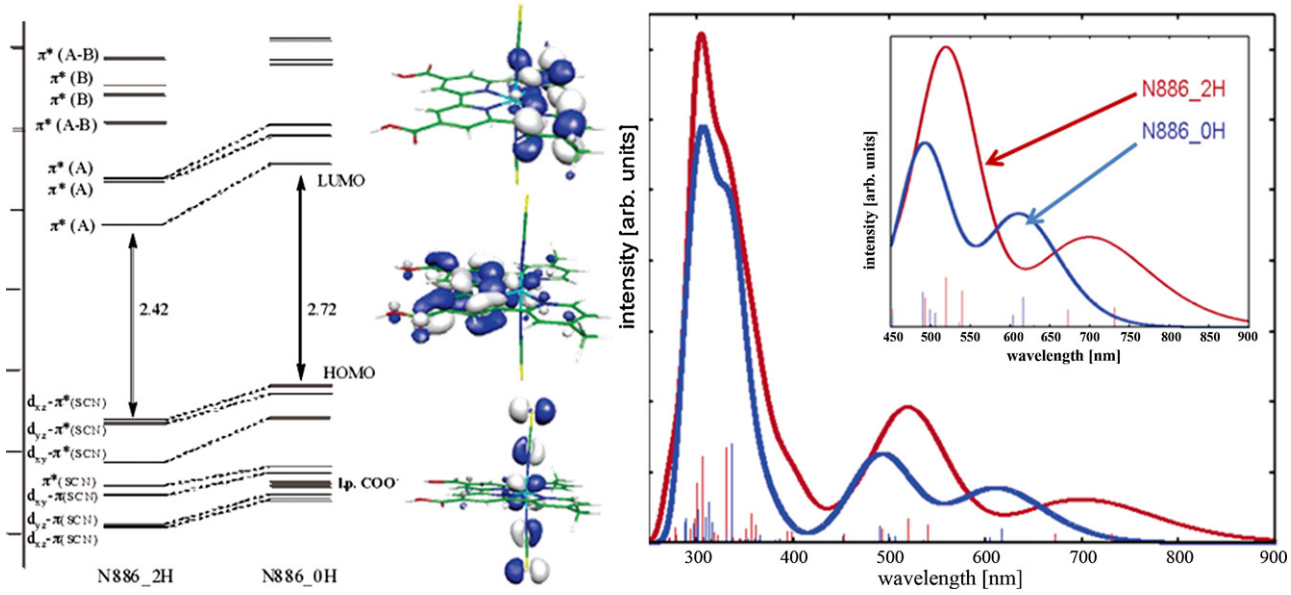

Fig. 7. Left: Molecular orbital energies and character for the protonated and deprotonated N886 complex, along with isodensity plots of selected molecular orbitals. Right: Calculated absorption spectra for the protonated (red) and deprotonated (blue) N886 complex in ethanol solution. Inset: a detail of the low energy spectra region. Adapted from Ref. [48].

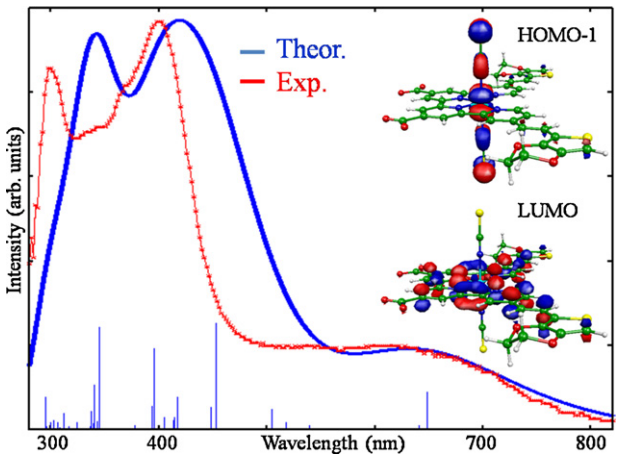

Fig. 8. Comparison between the experimental absorption spectrum of N1044 (red line) and the calculated one for the deprotonated complex (blue line). The calculated spectrum has been obtained by a Gaussian convolution with FWHM = 0.45 eV. The intensity of the experimental spectrum has been rescaled to match that of the calculated feature of the deprotonated complex at 410 nm.
Reproduced from Ref. [51] by permission of The Royal Society of Chemistry.

respectively. The ESOP for the protonated complex is rather close to the TiO_2 conduction band [74], suggesting an unfavorable energetics for electron injections.

2.6. Ru(II) dyes on TiO_2: adsorption and excited states

To the best of our knowledge, the first computational investigation from first principles reported on an inorganic dye on TiO_2 was performed by us in 2004 [85]. In this case, we investigated the electronic structure, adsorption geometry and optical absorption spectra of $[Fe(CN)_6]^{4-}$ on a $(TiO_2)_{38}$ cluster of nanometric dimensions. The first DFT investigation of a Ru(II)-dye adsorbed onto TiO_2 was reported by Persson et al. in 2005 [86a]. The calculation was based on the adsorption geometry previously reported for bis-isonicotinic acid by the same authors [86b]. The adsorption mode was therefore occurring via a single bipyridine ligand, which was binding to TiO_2 in a bidentate dissociative way. The N3@TiO_2 electronic structure is in many ways similar to that calculated for free dyes. The few highest occupied orbitals are located near the middle of the substrate band gap and are seen to be localized on the dye. The lowest few unoccupied dye orbitals are close in energy to the TiO_2 conduction band edge. The LUMO and LUMO+1 of the combined system are largely located on the two N3 functionalized bipyridine ligands. More recently, the Persson group reported a theoretical investigation of bis-terpyridine Ru(II)-dyes adsorbed onto a $(TiO_2)_{46}$ cluster, investigating the adsorption mode and electronic coupling strength of various $[Ru(tpy)_2]^{2+}$ dyes, bearing both carboxylic and phosphonic acid groups, with or without the presence of a phenylene spacer [87]. This study provided a clear evidence that the interfacial coupling strength is significantly affected by the presence of both anchor and spacer groups.

In an effort to optimize the overall device conversion efficiency, it was found that the photocurrent (i_{ph}) and the open-circuit voltage (V_{OC}) significantly increases and decreases, respectively, by increasing the number of protons carried by the sensitizer's carboxylic groups. Optimal performances were obtained for dyes carrying 1–2 protons over a possible range of 0–4 [45,88]. Since some of the sensitizer's protons can be transferred to the TiO_2 surface [88], these observations suggest that protonation of the sensitizer and/or of the surface can have an important influence on the electronic dye/semiconductor coupling and on the position of the TiO_2 conduction band in DSCs [89].

Motivated by these observations, we reported a TDDFT investigation of the adsorption geometry and excited states of the N719 dye on TiO_2 [88]: two adsorption configurations were optimized, which differed for the position of the two protons initially carried by the dye. In one case the protons were retained on the dye (A in Fig. 9) while in the other case (B) they were both transferred to the surface. TDDFT calculations (B3LYP/3-21G*) in solution were thus performed on the Car-Parrinello optimized geometries, simulating the absorption spectra of the A and B systems.

Dye adsorption takes place via two carboxylic groups residing on different bipyridine ligands, even though, due to the limited TiO_2 cluster size, we could not assess the feasibility of adsorption through a third carboxylic group. Configuration B in Fig. 9, was substantially more stable than A, suggesting that protons can be effectively transferred from the dye to the surface. For both A and B, the computed electronic structure shows that the N719 HOMOs fall within the TiO_2 band gap. Significant differences between the A and B configurations are instead found in the energy and character of the LUMOs. In particular, adsorption of the two protons onto the TiO_2 surface in B leads to a downshift of the manifold of unoccupied orbitals by about 0.15 eV compared with A, consistent with the experimentally measured V_{OC} reduction observed for DSCs employing dyes containing 0–2 protons [45,89]. In addition, our results unambiguously show that, associated with this energy down-shift, there is a considerable mixing of the sensitizer π^* orbitals, delocalized across the carboxylic-substituted bipyridine ligands, with conduction band states of the TiO_2 nanoparticle, see Fig. 10. While in A the LUMO/LUMO+1 are pure N719 π^* orbitals followed at higher energy by pure TiO_2 conduction band states, in B the LUMO/LUMO+3 are mixed N719/TiO_2 states [88].

A comparison between the calculated absorption spectra for A and B and the experimental spectrum for N719-sensitized TiO_2 is reported in Fig. 10. The spectroscopic shapes calculated for A and B do not show significant differences and, although slightly red-shifted and broader, are both in good agreement with the experiment. For A, the absorption spectrum is dominated by an intense transition at 2.19 eV essentially corresponding to the dominant MLCT transition of N719 in solution, found at 2.38 eV. The resulting excited state is only weakly energetically and spatially coupled to the TiO_2 conduction band thus a reduced rate of electron injection from the dye to TiO_2 is to be expected. For B, the absorption spectrum is characterized by two main excitations at 1.98 and 2.45 eV involving, as arriving states, mixed dye-TiO_2 orbitals, see Fig. 10. This suggests that in B the dye excited states are strongly coupled to the TiO_2 conduction band giving potentially rise to large rates of electron injection. Our study pointed out that two different electron injection mechanisms may be present in DSCs employing dyes carrying a different number of protons: an adiabatic injection mechanism, in which the same electronic state changes its localization from the dye to the TiO_2, and a non-adiabatic electron injection mechanism, in which the photoexcited electron tunnels from the dye to the TiO_2 conduction band.

Another important aspect which we addressed by our calculations concerns the possible dependence of the DSCs open circuit potential (V_{OC}) from the nature of the dye. The relation between the dye structure and the V_{OC} is not straightforward, since this quantity essentially depends on the recombination rate between TiO_2-injected electrons and oxidized species in the electrolyte and on the position of the TiO_2 conduction band. Quite unexpectedly, experiments have shown that V_{OC} for DSCs employing heteroleptic dyes is significantly lower compared to that observed using homoleptic sensitizers containing the same number of protons [90]. This difference is likely to originate from the different adsorption modes of the two types of complexes onto the TiO_2 surface. Indeed,

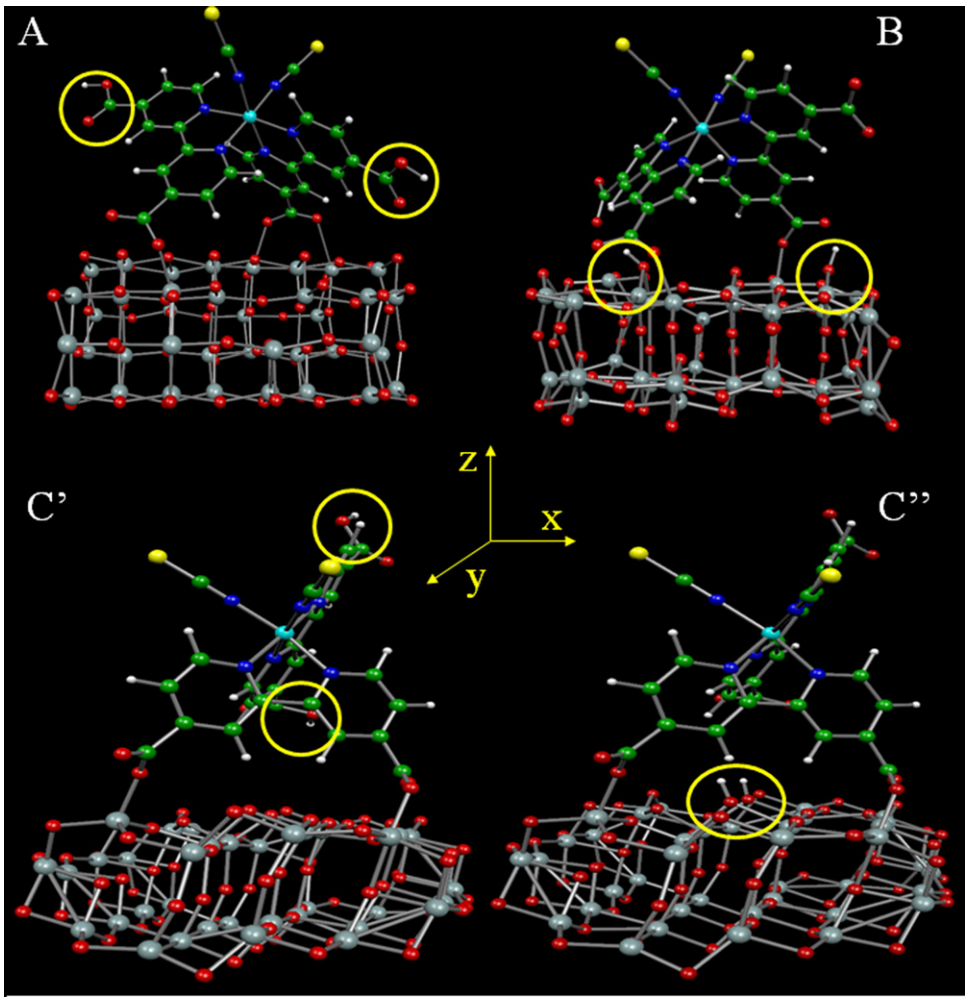

Fig. 9. Optimized molecular structures of the N719 dye adsorbed onto the $(TiO_2)_{38}$ cluster. Upper Left: A configuration, where the two dye protons are retained on the dye. Upper Right: B configuration, where the protons are both transferred to the TiO_2 surface. Bottom C′ and C″ configurations, in which adsorption is through a single bipyridine. The circles indicate in both cases the positions of the protons.
Reprinted with permission from reference [90]. Copyright 2011 American Chemical Society.

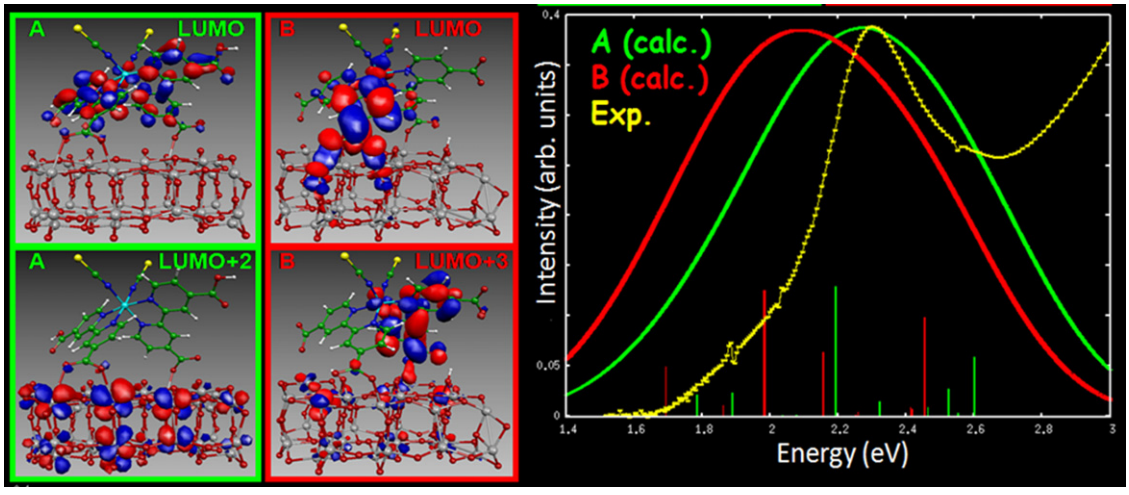

Fig. 10. Left: plots of relevant LUMOs for A (left) and B (right). Right: comparison between computed absorption spectra for A (green) and B (red) and experiment for N719-sensitized DSSCs (yellow). Vertical lines indicate the calculated excitation energies and oscillator strengths. A gaussian broadening with $\sigma = 0.25$ eV was used to simulate the theoretical spectra. The spectra have been rescaled to show the same peak intensity.
Reprinted with permission from Ref. [88]. Copyright 2011 American Chemical Society.

while homoleptic dyes, such as N3 or N719, can adsorb on TiO_2 using carboxylic anchoring groups residing on different bipyridine ligands, heteroleptic dyes, e.g. N621 or Z907, necessarily adsorb via carboxylic groups residing on the same bipyridine. We therefore investigated the origin of the different V_{OC} by means of DFT calculations on representative homoleptic and heteroleptic dyes adsorbed on TiO_2 in different configurations [90]. In addition to the A and B configurations reported in Fig. 9, we also considered adsorption through deprotonated (protonated) carboxylic groups belonging to the *same* bipyridine, C′ and C″, respectively, in Fig. 9. While the HOMOs of the four investigated configurations do not show appreciable differences, remarkable differences are found in the energies and character of the LUMOs depending on the position of the two protons and the sensitizer's adsorption geometry. Our calculations have shown that, besides protonation, also the sensitizer's adsorption mode affects the position of the TiO_2 conduction band edge. For a given number of protons (0 or 2) transferred to the surface, the systems where the sensitizer is adsorbed via a single bipyridine ligand have the TiO_2 conduction band edge at significantly lower energies with respect to the systems in which the sensitizer is adsorbed through two different bipyridine ligands. These results support the idea that the sensitizer adsorption mode is the origin of the reduced V_{OC} values experimentally observed for heteroleptic sensitizers, possibly in relation to the sensitizer dipole [90]. We later confirmed that the sensitizer dipole effectively shifts the TiO_2 conduction band edge in solid-state DSC devices [91].

Recently, with the aim of correlating cell efficiency parameters to the properties of the dye@TiO_2 interfaces, we performed an extensive study on the N719 adsorbed on TiO_2 [92]. Along with the dipole effects mentioned above, a possible reason of the high open circuit potential exhibited by N719 may be that the (two to four) carboxylic groups in contact with the TiO_2 semiconductor surface charge it negatively, thus shifting the TiO_2 conduction band to higher energy. A further possibility is that, due to its adsorption geometry, N719 could form a denser monolayer on the TiO_2 surface, compared to other heteroleptic dyes. This property may reduce the recombination of TiO_2-injected electrons with the oxidized electrolyte by preventing the I_3^- anions from approaching the semiconductor surface, thus further enhancing the open circuit potential (recombination reduces the electron density into the titania, thus lowering the device Fermi level) [90,91]. The relevance of the anchoring mode on the photovoltaic performances of Ru(II) dyes is also supported by a recent study on the homoleptic cyclometalated YE05 dye [83], which delivers a DSCs open circuit potential of ∼800 mV, close to the value of ∼850 mV characteristic of highly optimized N719-based DSCs [83]. Altogether, the above observations provide evidence that the N719 dye adsorption mode onto TiO_2 is a key ingredient to its success. DFT-based molecular dynamics simulations and electronic structure calculations aimed at establishing the detailed adsorption geometry of the N719 and YE05 dyes on TiO_2 were performed. A large $(TiO_2)_{82}$ model was employed in this study, to minimize the impact of the cluster dimensions on the calculated properties [92]. Single point calculations (B3LYP/3-21G*) in solution were performed, explicitly including the dye counterions, either the real tetrabutyl ammonium (TBA) or Na^+ counterions carried by the N719 dye. We have shown that the N719 and YE05 dyes, both bearing two bipyridine ligands functionalized with four carboxylic groups, adsorb onto the TiO_2 surface by exploiting *three* carboxylic groups, Fig. 11. The two protons initially carried by the N719 dye are transferred to the semiconductor surface, even though one of the two protons is actually shared between the dye and a nearby TiO_2 surface oxygen. The related YE05 dye exhibits the same adsorption geometry as N719. In a subsequent investigation Schifmann et al. reported molecular dynamics simulations of N3 on TiO_2, finding dye adsorption via three carboxylic groups to be energetically favored [93]. For the N719- and YE05-sensitized systems an almost identical TiO_2 conduction band energy and shape was calculated, see Fig. 11, suggesting that the high open circuit potential observed in DSCs employing the two sensitizers might be effectively related to their adsorption geometry.

3. Ir(III)-complexes as phosphorescent emitters for OLEDs

OLEDs are very promising devices which efficiently convert electricity into light through the process of electroluminescence. They are made by depositing an active layer of a few tens or hundreds of nanometres thickness between two flat electrodes: one transparent electrode which is used as anode, and an electrode with a low work function used as cathode. Different classes of material can be used as active layers, ranging from polymers to fluorescent or phosphorescent molecules. OLEDs are a very versatile type of technology having a wide range of applications and are characterized by low embodied costs. To date OLEDs based on phosphorescent materials achieved among the highest reported efficiency. Due to spinorial statistics involving both singlet and triplet excitons, charge carriers injected into the device have a larger probability of recombining and emitting light than in the case of fluorescent compounds, where only singlet excitons can be gathered. Ir(III) cyclometalated complexes are attracting wide spread interest as emitters in OLEDs and light-electrochemical cells (LECs) because of their unique photophysical properties. The success of these complexes is related to their high stability, emission color tunability, and strong spin–orbit coupling, which sharply increases the efficiency of radiative transitions. OLEDs and LECs emitters should present sharp colors in the red, green, and blue region, exhibiting at the same time very high phosphorescence quantum yields. Cyclometalated Ir(III) complexes have been successfully used for OLED applications because of their high triplet quantum yields [94,95], which are the result of various factors, including the large d-orbital splitting, the close lying proximity of π–π^* and MLCT states, and the strong spin–orbit coupling introduced by the heavy metal [96].

In 2004 the first ionic cyclometalated Ir(III) complex [Ir(ppy)$_2$(4,4′-di-*tert*-butyl-2,2′-bipyridine)][PF_6] (**1** in Fig. 12) (where ppy is the cyclometalated 2-phenylpyridine ligand), was used in electroluminescent devices [97]. From that time, large efforts have been devoted to tune the emission spectrum by opportunely substituting and/or functionalizing the cyclometalated and ancillary ligands. In mixed ligand Ir(III) cationic complexes, the different ligands can be almost independently functionalized, thus achieving the desired emission color by selective tuning of the HOMO and LUMO energies. Moreover, the use of cationic complexes, bearing drifting counterions, allows the use of a simplified device architecture [97]. Several groups have extensively used neutral iridium cyclometalated complexes in OLED devices and obtained up to 19% external quantum efficiencies; the use of neutral iridium complexes, however, requires a complicated multilayered structure for charge injection, transport, and light emission [7–10]. In contrast to neutral and cationic complexes, anionic Ir(III) complexes have received little attention, despite the considerably high quantum yield exhibited by such systems [10,55].

Here we present an overview of DFT/TDDFT results obtained for selected cationic, neutral and anionic iridium complexes. The common aim of these investigations has been to individuate a relationship between the molecular structure of the Ir(III) complexes and their electronic, absorption and emission properties, thus aiding the design of new luminescent systems with improved characteristics. A survey of the investigated complexes is reported in Fig. 12.

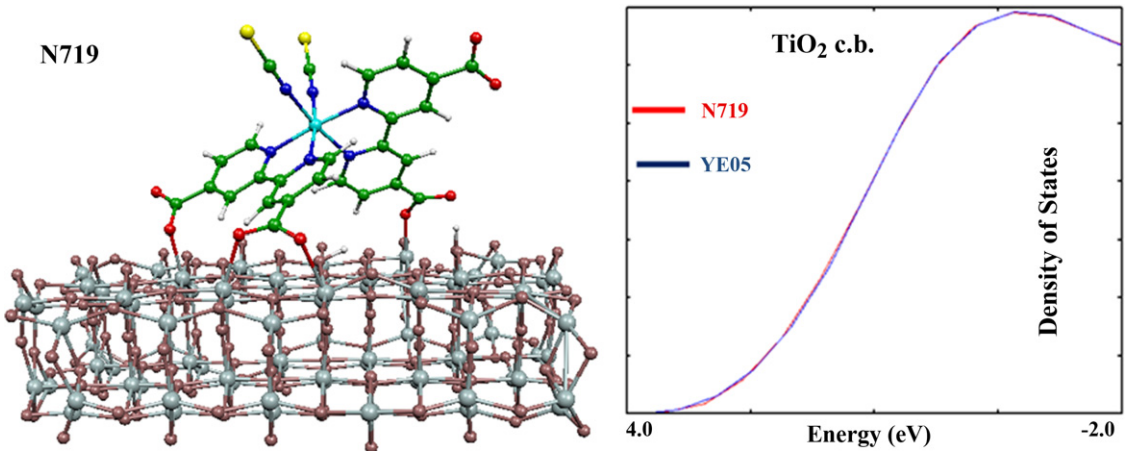

Fig. 11. Left: Optimized molecular structure of the N719 dye on TiO_2. Right: Density of states in the region of the TiO_2 conduction band for N719 (red line) and YE05 (blue line) systems. Notice that the two lines are almost indistinguishable.
Adapted from Ref. [92].

3.1. Cationic Ir(III) complexes

The investigated mixed ligand cationic $[Ir(C\hat{N})_2(N\hat{N})]^+$ complexes, with (CN̂) ppy and (NN̂) functionalized bpy or phenanthroline (phen) ligands, are characterized by tunable color and emission quantum yield by varying the electron withdrawing/releasing character of the two types of ligands. For this class of complexes, it was observed that electron withdrawing substituents on the (CN̂) ligands decrease the donation to the metal and therefore stabilize the metal-based HOMO, while electron releasing substituents on the (NN̂) ligand, destabilize the (NN̂) ligand-based LUMO, ultimately leading to increased HOMO–LUMO gaps and emission energies. Much less clear are the factors which determine the emission quantum yields in mixed ligand cationic complexes and on which parameters to act in order to increase them.

To obtain the desired green/blue emission, starting from the parent Ir(III) complex **1** [97], the tert-butyl groups of the bipyridine ligand have been substituted with the stronger electron donor groups, $-N(CH_3)_2$ thus obtaining $[Ir(2\text{-phenylpyridine})_2(4,4'\text{-dimethylamino-}2,2'\text{-bipyridine})](PF_6)$, **2** in Fig. 12 [55,56], and subsequently the electron withdrawing fluoride substituents have been inserted in the ppy ligand, leading to $[Ir(2,4\text{-difluorophenylpyridine})_2(4,4'\text{-dimethylamino-}2,2'\text{-bipyridine})](PF_6)$, **3,** see Fig. 12, for which a room-temperature solution photoluminescence quantum yield of 80–85% was reported [55]. Among the cationic complexes investigated with phenanthroline-substituted ligands, here we report on complexes of type $[Ir(ppy)_2(5\text{-X-}1,10\text{-phen})][PF_6]$ with X = Me, NMe_2 and NO_2, **4**, **5** and **6** in Fig. 12, respectively, which show a wide variety of emission colors and quantum yields depending on the phenanthroline substituent [56].

Geometry optimization of the singlet ground state (S_0) of the investigated **1**–**6** complexes, including relativistic effects, led to structures in excellent agreement with experimental data for the complex $[Ir(2\text{-phenylpyridine})_2(4,4'\text{-}C_9H_{19}\text{-}2,2'\text{-bipyridine})]^+$, for which X-ray data are available [98]. The effect of solvation on the calculated structural parameters is in all cases rather small. Starting from the optimized S_0 geometries and imposing a triplet spin multiplicity, we calculated the geometry of the lowest triplet excited state (T1). The geometrical variations observed for the triplet state mainly involve the bridging C–C bond of the bpy (phen) ligand and to a minor extent the Ir–$N_{(bpy)}$ (Ir–$N_{(phen)}$) and Ir–C distances, suggesting that the investigated ligands form a rigid scaffold around the metal center with strong metal-ligand interactions. For **1**–**3**, a considerable shortening of the C–$C_{(bpy)}$ (C–$C_{(phen)}$) distance is observed in T_1 compared to S_0, in line with the electronic structure we will discuss below, showing a LUMO localized within the bpy (phen) ligand of bonding character with respect to the C–$C_{(bpy)}$ (C–$C_{(phen)}$) bond. We also remark that for complex **2** the geometrical variations observed on going from S_0 to T_1 are essentially the same considering an SCF or TDDFT optimized geometry (B3LYP/SVP) for the lowest triplet excited state [55].

A survey of the electronic structure of complexes **1**–**3** is reported in Fig. 13 [55]. The HOMO of the three complexes is an anti-bonding combination of Ir(t_{2g}; d_{xy}) and ppy(π) orbitals. The HOMO of **3** is stabilized compared with that of **1**–**2** due to the presence of fluoride substituents on the phenyl ring, which act as electron acceptors. The contribution of Ir orbitals to the HOMO ranges from 44.8% to 46.8%. For **2** and **3** the HOMO is followed, in order of decreasing energy, by two almost degenerate combinations of Ir(t_{2g}; d_{xz}–d_{yz}) and π orbitals of the 4,4′-bis(dimethylamino)-2,2′-bipyridine ligand, which are missing in **1**. The LUMO of the three complexes is a π^* orbital localized on the substituted bipyridine ligand and is calculated to lie at −2.49, −2.03 and −2.14 eV for **1**–**3**, respectively. At higher energy the LUMO is followed by an almost degenerate couple of (substituted) ppy π^* orbitals, whose energy approaches that of the substituted bipyridine π^* LUMO on going from **1** to **3**. The HOMO–LUMO gaps increase substantially on going from **1** to **3**, reflecting the HOMOs and LUMOs stabilization and destabilization, respectively, taking place in **2** and **3** compared to **1**.

The electronic structure of the cationic complexes **4**–**6** is schematized in Fig. 14 [56]. For complexes **4**–**6** the HOMO has the same Ir(t_{2g}) and ppy(π) antibonding character as for **1**–**3**. For complex **5** the HOMO−1 is a π-bonding orbital of the NMe_2-substituted phenanthroline which lies close to the HOMO, as a result of the increased electron donation of the NMe_2 group on the phenanthroline ring. The LUMO of **4**–**6** is a π^* orbital localized on the phenanthroline ligand. For **4** and **5** the LUMO is followed by a second phenanthroline π^* orbital (LUMO+1), whose energy relative to the LUMO depends upon the substituent, and at higher energies by a couple of almost degenerate ppy π^* orbitals. This electronic structure is not qualitatively affected by changing the solvent, even though a general energy down-shift of both occupied and unoccupied orbitals is calculated for dichloromethane compared to acetonitrile.

A comparison of calculated and experimental absorption spectra for **2** and **3** are reported in the left and right upper panels, respectively, of Fig. 15. The experimental spectra of the two complexes show intense features below 300 nm and less intense features in the range 300–400 nm with tails which extend

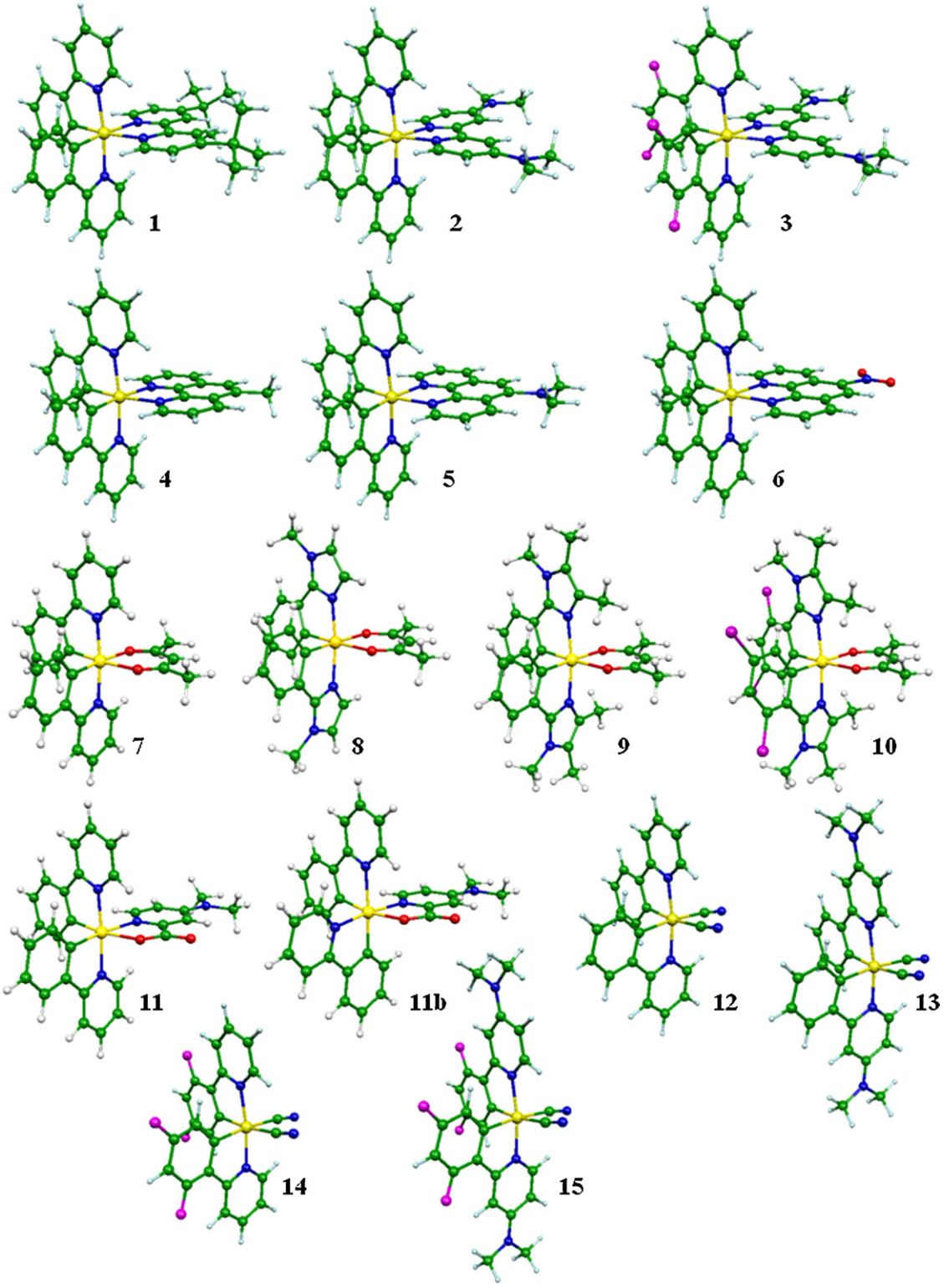

Fig. 12. Optimized molecular geometry of selected cationic (**1**–**6**), neutral (**7**–**11b**) and anionic (**12**–**15**) Ir(III) complexes.

into the visible region. It needs to be stressed that within the computational approach used here singlet–triplet excitation energies have zero oscillator strengths, because of the neglect of spin–orbit coupling in the TDDFT calculations. To perform a comparison of the experimental and calculated spectra in wavelength regions dominated by low-lying singlet–triplet transitions we report as insets of Fig. 15 the low-energy portions of the spectra, including the calculated values of singlet–triplet excitations.

Considering the approximations described above, the agreement between the calculated and experimental spectra is quite good. We are indeed able to reproduce the appearance of the main spectroscopic features and their relative intensities, even though the calculated spectra appear to be slightly blue-shifted and for **3** we are partly underestimating the intensity in the 300–350 nm region. For **2** at longer wavelengths we calculate three transitions of sizable intensity at 345, 384 and 417 nm which can be related

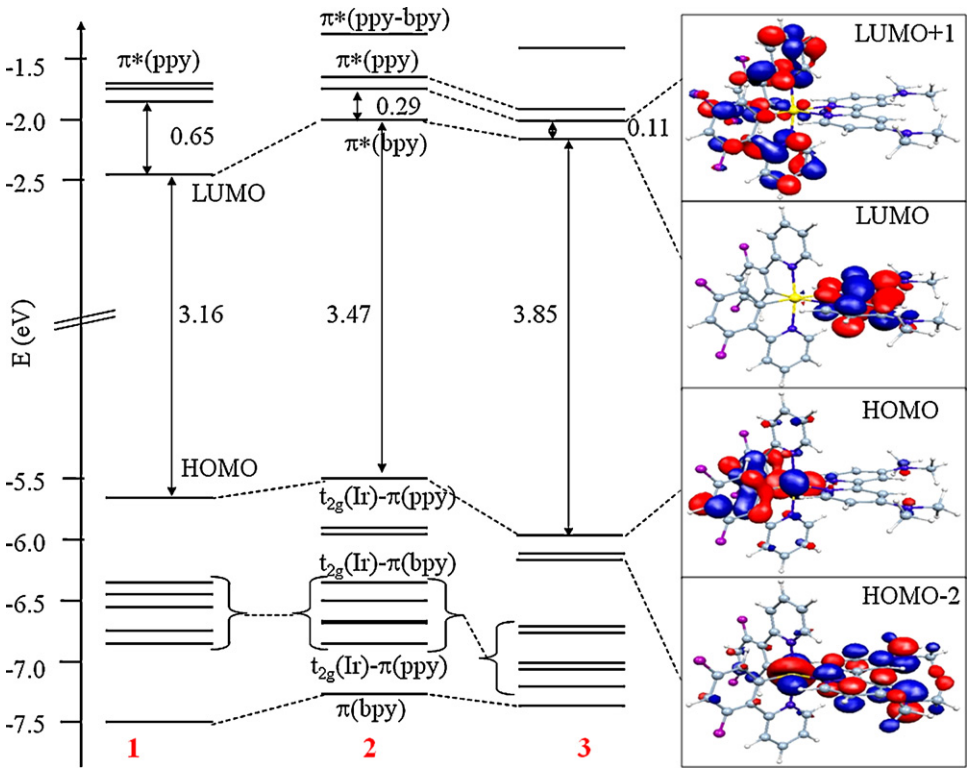

Fig. 13. Calculated electronic structure in acetonitrile solution for complexes **1**–**3** at their S_0 optimized geometries. Also shown are isodensity surface plots of selected molecular orbitals of complex **3**.
Reprinted with permission from reference [55b]. Copyright 2011 American Chemical Society.

to the 355, 375 and 417 nm features of the experimental spectrum, see inset of Fig. 15. These three transitions have mixed π–π* and MLCT character, having the ppy π* the bpy π* LUMOs as arriving states.

To gain insight into the origin of the weak band experimentally found at 472 nm we looked at singlet–triplet excitations, reported in the inset of Fig. 15; we can relate the 472 nm band to the presence of two singlet–triplet excitations calculated at 462 and 461 nm. These two transitions have mixed π–π* and MLCT character with arriving π* states localized on the bpy and ppy ligands, respectively. The absorption spectrum of **3** is rather similar to that of **2** and similar bands assignments hold. Also in the **3** case we assign the weak band experimentally found at 444 nm to almost overlapping singlet–triplet excitations calculated at 438 and 437 nm with bpy and ppy π* arriving states. For the cationic complexes **4**–**6** a similar assignment of the main absorption features as for **2**–**3** holds [56]. Also in this case the agreement between theory and experiment is good, both in terms of absolute band posi-

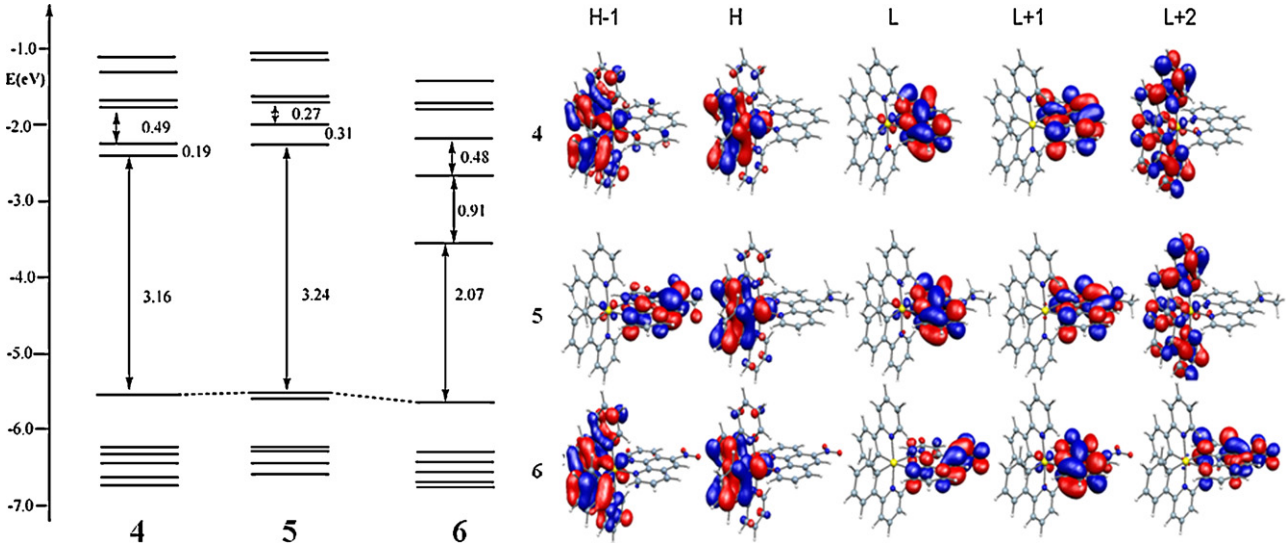

Fig. 14. Schematic representation of the frontier molecular orbitals of complexes **4**–**6** along with isodensity plots of their molecular orbitals.
Reprinted from Ref. [58]. Copyright 2011 with permission from Elsevier.

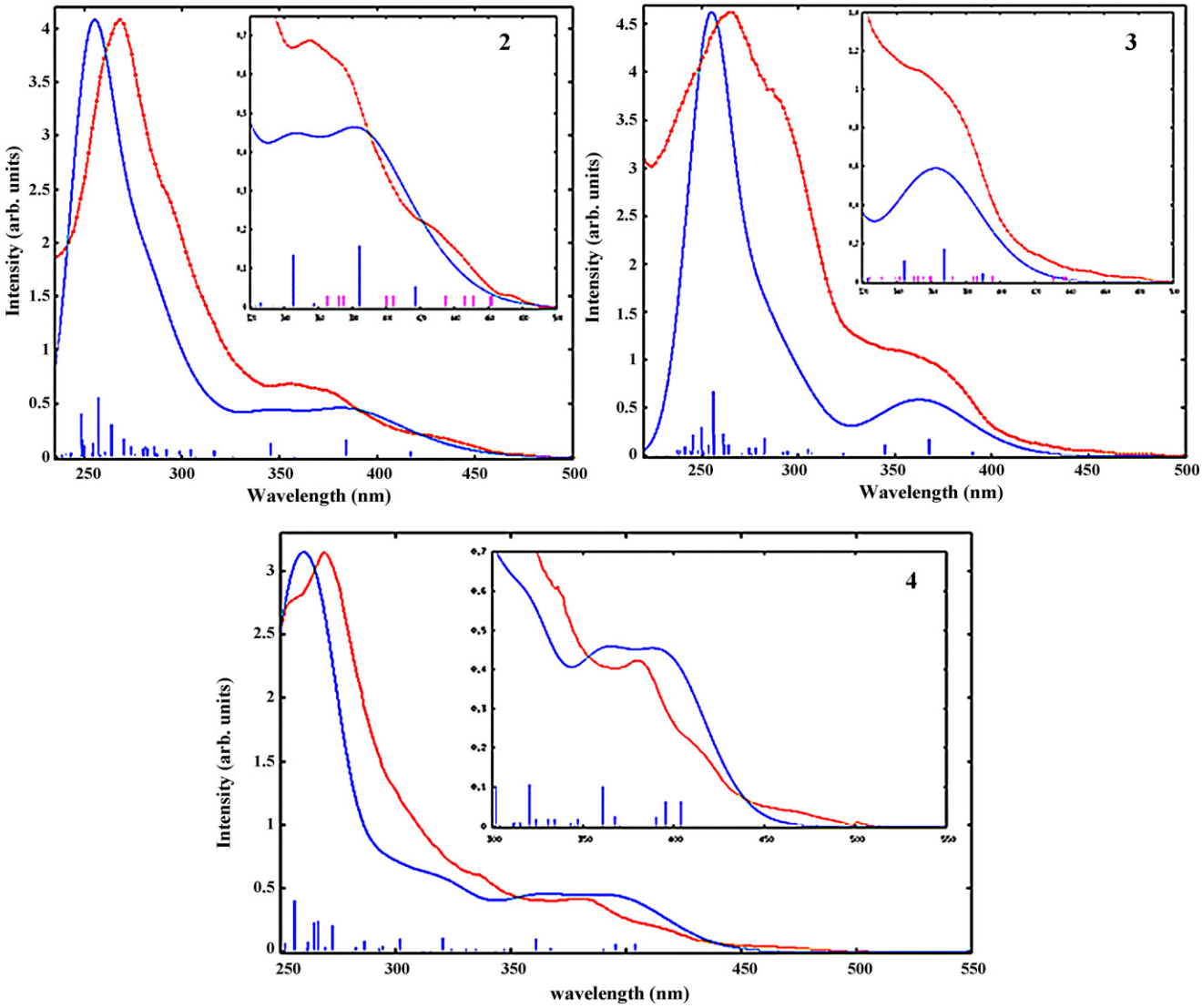

Fig. 15. Comparison of the calculated (blue line) and experimental (red line) absorption spectra of **2** (left upper panel) and **3** (right upper panel) and **4** (lower panel) in acetonitrile solution. Blue vertical lines correspond to unbroadened oscillator strength of calculated singlet–singlet transitions. The insert shows a detail of the low-energy spectra region, with both singlet–singlet (blue vertical lines) and singlet–triplet calculated transitions (magenta vertical lines), the latter with arbitrary intensity to indicate their positions.
Adapted from Ref. [58].

tions and relative intensities, see **4** in the lower panel of Fig. 15.

To gain insight into the nature of the excited states involved in the emission process, we performed the calculation of the lowest singlet–singlet and singlet–triplet excitation energies at the optimized geometries of the lowest triplet states. The emission spectra of **2** and **3** in dichloromethane are quite similar, showing two main peaks at 491/520 and 463/493 nm (2.68/2.51 and 2.53/2.38 eV), respectively, Fig. 16. On the other hand the emission spectrum of **1** is characterized by a broad unstructured emission centered at 581 nm (2.13 eV). Also, for the cationic complex **4**, bearing a substituted phenanthroline ligand, the emission spectrum is broad and unstructured with a maximum at 559 nm (2.22 eV). Compounds **5**–**6** are only weakly emissive.

The calculated emission energies nicely correlate with the experimental data for **1**–**3**. In particular, a considerable blue-shift of the lowest excitation energies is calculated on going from **1** to **3**. Our calculations show that at the S_0 and T_1 geometries the lowest triplet excited states of the three complexes are localized on the bpy ligands. We also notice that while for **1** the lowest triplet state is originated by a single HOMO → LUMO excitation, for **2** and **3** the lowest triplet state has components from lower-lying orbitals, thus showing an increased bpy intraligand contribution compared to **1**. For complex **4** the calculated emission is assigned to as a HOMO–LUMO triplet transition, involving therefore the substituted phenanthroline ligand.

Comparison of calculated emission energies with emission spectroscopic maxima is not always straightforward, since the emission intensities are determined, for a given couple of electronic states, by vibrational wavefunction overlaps (the Franck–Condon factors) between the excited state lowest vibrational level and the various vibrational levels of the ground state. Explicit calculation of the emission lineshape and of E_{0-0} value becomes therefore very important. By applying the procedure outlined in Ref. [99], we calculated the lineshape of the emission spectra of **2** and **3** and compared them to the experimental spectra in Fig. 16 [100].

The experimental spectra of **2** and **3** show a broad two-peak shape as a consequence of the inhomogeneous broadening induced

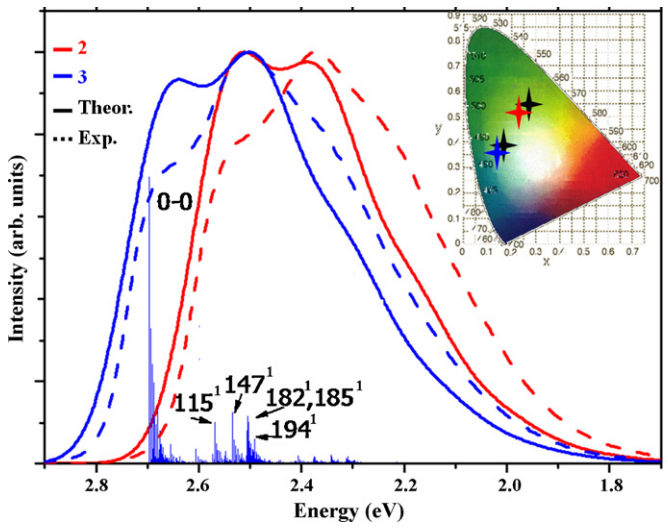

Fig. 16. Calculated (solid lines) and experimental (dashed lines) emission spectra for **2** (red) and **3** (blue), along with calculated stick-spectrum for **2** (blue vertical lines). The calculated (blue/red stars) and experimental (black stars) CIE coordinates for **3** and **2** are also shown. Vibrational contributions are labeled by n^x, where x indicates the quanta deposited on normal mode n and the modes not explicitly mentioned are in their ground state ($x = 0$).
Reprinted with permission from Ref. [100]. Copyright 2011 American Chemical Society.

by the polar solvent. Apart from a 0.24 eV shift, the agreement between theory and experiment is good and the main experimental spectroscopic features are accurately reproduced, except for a slight overestimation of the intensity of the E_{0-0} transition. Most notably, having accurately calculated the band shape, we can provide a computational estimate of the CIE color coordinates for the investigated complexes. With reference to data in Fig. 16, our calculations lead to 0.19:0.34:0.47 CIE coordinates for **3**, to be compared with experimental values of 0.21:0.39:0.41. Furthermore, it is apparent that our calculations quantitatively reproduce the difference in CIE coordinates between **2** and **3**, hence the different emission color.

3.2. Neutral Ir(III) complexes

The use of different ancillary ligands allows further tuning of the band shape and emission maximum of Ir(III) cyclometalated complexes. Neutral Ir(III) complexes bearing acetylacetonate (acac) ligands have been extensively studied, emphasizing the effect of tuning both the ppy and the acac ligands on the optical properties. In particular, considering the (acetylacetonato)bis(2-phenylpyridine)iridium(III), [Ir(ppy)$_2$,acac], **7** [101], as reference, the (acetylacetonato)bis(1-methyl-2-phenylimidazole)iridium(III), **8** [59] and the related **9** and **10** complexes, which are methyl substituted imidazole and chloride substituted phenyl, respectively, have been investigated. Complex **8** (also known as N966) has proved to be particularly interesting, exhibiting white photo- and electro-luminescence [59]. To provide insight into the electronic structure and the optical properties of complex **8** we performed DFT/TDDFT calculations on its ground singlet and on its two lowest triplet excited states (T_1 and T_2, respectively). We compared the electronic and optical properties of **8** and the well known **7**, [Ir(ppy)$_2$acac], complexes, the latter showing green luminescence with a much less broad emission spectrum [101]. The two complexes share the same HOMO of Ir(t_{2g};d_{xy})–ppy(π) character. For **7** the LUMO/LUMO+1 are degenerate π^* orbitals of the ppy ligands, followed at higher energy by a second degenerate couple of antibonding orbitals localized on the ppy and acac ligands (LUMO+2 and LUMO+3, respectively). For **8**, the LUMO is a π^* orbital delocalized over the cyclometalated ligands. However, in relation to the destabilization of this orbital due to the increased donor capability of the bis(1-methyl-2-phenylimidazole) ligands, a considerable mixing of the cyclometalated and acac-based π^* orbitals in the LUMO+1 and LUMO+2 occurs. This provides a set of three almost degenerate LUMOs, Fig. 17.

In **7** the S_0–T_1 and S_0–T_2 transitions are almost degenerate (482 and 479 nm), reflecting the degeneracy of the phenylpyridine based LUMO/LUMO+1. The lowest triplet transition involving the acac-based LUMO+3 is calculated at higher energy, reflecting the molecular orbital energies discussed above. In **8** the lowest S_0–T_n transitions, are, on the other hand, found at essentially the same wavelength (440, 433 and 431 nm, respectively); recalling the degeneracy and character of the three N966 LUMOs, our data indicate comparable contributions to the lowest excited states by the cyclometalated and acac ligands. This degeneracy is only partly resolved at the excited state relaxed geometries, for which we still calculate the two lowest excited states to lie within ca. 0.1 eV. This is opposed to the [Ir(ppy)$_2$acac] case for which calculations performed at the T_1 geometry indicate that the acac-based lowest triplet state is very energetically separated from the ppy-based lowest excited state (0.58 eV).

The proximity of the lowest cyclometalated- and acac-based excited states in **8** is opposed to well characterized ppy-based emission found in **7**, suggesting the origin for the broad emission spectrum observed for **8,** Fig. 17.

Several neutral Ir(III) complexes have been recently developed starting from **8**, with complex **9** showing a completely methylated imidazole ligand, and complex **10** being originated from **9** by inserting chloride substituents in **2** and **4** positions of the phenyl ring [102]. Chlorine should acts as an acceptor group and therefore a blue shift of the emission maximum could have been expected. Surprisingly, however, the chlorine substitution induces more than 0.20 eV red shift of the emission maximum when compared to **9**. To provide insight into this counter-intuitive spectroscopic behavior, DFT/TDDFT calculations were performed on complexes **9** and **10**, by optimizing the geometry of both the ground singlet and lowest triplet excited states. A similar electronic structure was retrieved for **9** and **10**, Fig. 18, even though a slight reduction of the HOMO–LUMO gap was calculated for the latter. In line with this electronic structure picture, the lowest transition energies in **10** are red-shifted compared with those calculated for **9**. This behavior is particularly evident if one considers the excited states related to the emission process, i.e. the $S_0 \rightarrow T_1$ transitions calculated at the T_1 optimized geometries; in this case, a red-shift from 485 to 528 nm is calculated going from **9** to **10**. What is interesting to notice, in any case, is that transitions energies calculated for **9** and **10** at the triplet optimized geometries, show a much larger difference in energy (0.21 eV) than the corresponding quantities calculated at the singlet optimized geometries (0.08 eV), suggesting that a rather sizable geometrical and electronic relaxation accompanies formation of the emitting excited state in **10**.

We recently reported on the effect of the isomerization on the performances of an OLED devices. The [Ir(2-phenylpyridine)2(2-carboxy-4-dimethylaminopyridine)], N984 (**11**), isomerizes during the device preparation to the corresponding complex, N984b (**11b**) (see Fig. 12) with the pyridine rings of the cyclometalated ligands in *cis* position to each other [60]. Two devices, one containing pure **11** and one containing a mixture of **11** and **11b** as dopant in the emissive layer have been compared. Dramatic and inconvenient effects of the **11b** isomer on the device performances has been observed, even though the photo- and electro-chemical properties of the two isomers are very similar. To find a rational of this dissonant behavior we performed DFT/TDDFT calculations on the two

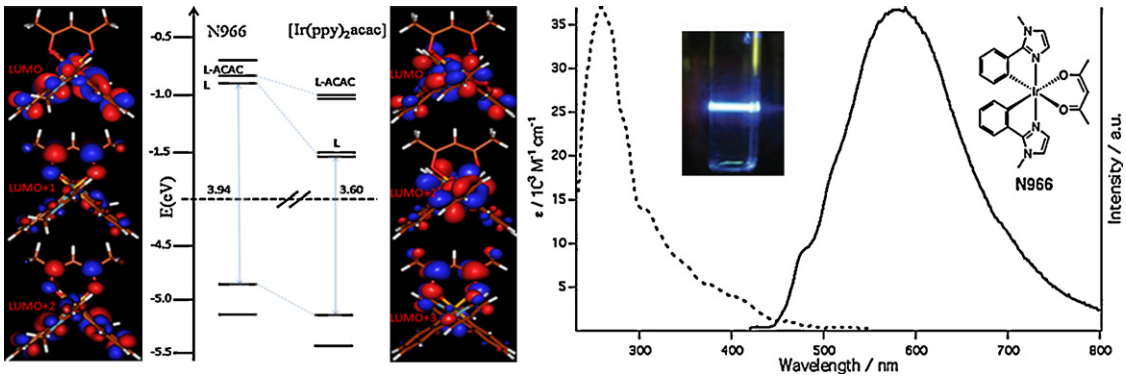

Fig. 17. Left panel: Schematic representation of the frontier molecular orbitals for the **8** and [Ir(ppy)$_2$acac] complexes calculated at the S_0 geometries. Plots of relevant unoccupied orbitals are also reported. Right panel: Experimental absorption (left dotted line) and emission spectra (right full line) of **8** in dichloromethane. The inset shows the chemical structure of N966. The photo shows the white-light emission of **8** obtained upon excitation using 355 nm laser light.
Reproduced from Ref. [59] by permission of The Royal Society of Chemistry.

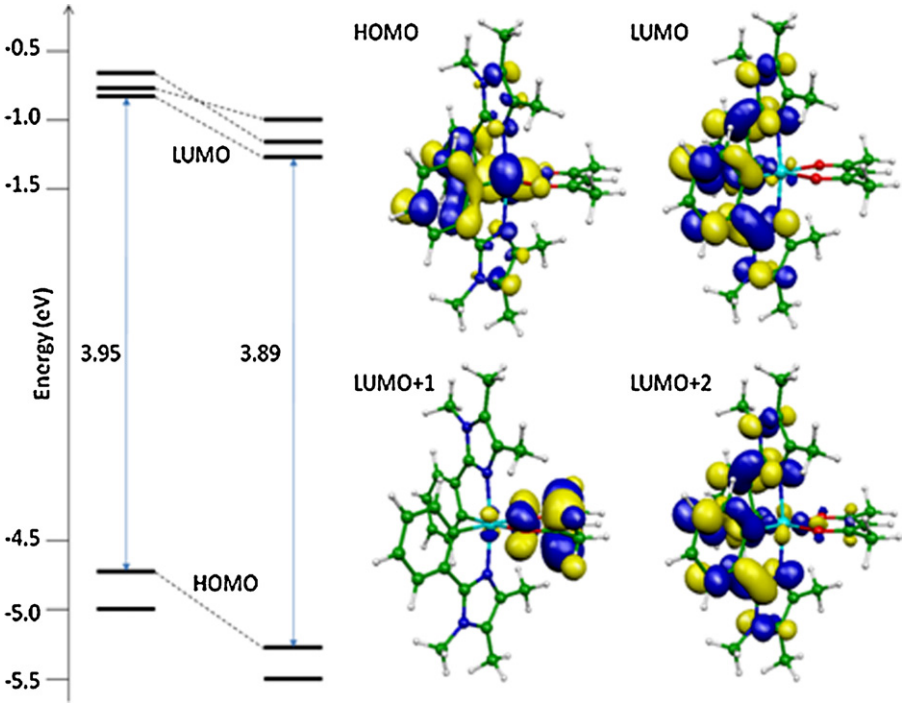

Fig. 18. Molecular orbital energy diagram for **9** and **10** and isodensity plots of selected orbitals for **9**.
Reprinted with permission from Ref. [102]. Copyright 2011 American Chemical Society.

Ir(III) complexes, **11** and **11b**. The frontier molecular orbitals of **11** and **11b** are displayed in Fig. 19.

The highest occupied molecular orbital (HOMO) of **11** is an almost isolated orbital composed by a combination of Ir(t_{2g})d_{xy} and π orbital on both the phenyl rings of the phenylpyridine ligands, with the HOMO−1 lying more than 0.5 eV below the HOMO. The HOMO of **11b** is somehow similar to that of **11** complex, albeit lying at slightly lower energy (0.1 eV), but the charge density shared between the metal and the phenylpyridine ligand is localized on a different plane. The most noticeable difference between **11** and **11b** is that in the latter the HOMO is followed within 0.2 eV by two close-lying orbitals, that in **11** are lying at considerably lower energy, see Fig. 19. This observation suggests that **11b** might be a better hole transporter than **11**, whereby the charge hole would be shared among the manifold of HOMOs in **11b**, while it would be trapped in the isolated HOMO, lying at higher energy, in **11**. Although quite speculative, this observation turns out to be consistent with the different device data obtained with the two isomers.

3.3. Anionic Ir(III) complexes

An alternative way to modulate the optical properties of Ir(III) cyclometalated complexes is to tune the HOMO–LUMO gap by inserting ancillary ligands, modifying at the same time the cyclometalated ligands [10,57]. This strategy has been recently used by us to produce the anionic complexes $(C_4H_9)_4N$[Ir(2-phenylpyridine)$_2$(CN)$_2$], **12**, $(C_4H_9)_4N$[Ir(2-phenyl-4-dimethylaminopyridine)$_2$(CN)$_2$], **13**, $(C_4H_9)_4N$[Ir(2-(2,4-difluorophenyl)-pyridine)$_2$(CN)$_2$], **14**, and $(C_4H_9)_4N$[Ir(2-(2,4-difluorophenyl)-4-dimethylaminopyridine)$_2$(CN)$_2$], **15**, with tunable color in the blue region of the spectrum and high solution quantum yields in the range 50–80%.[57] The anionic, neutral and cationic complexes investigated here share the same HOMO of Ir(t_{2g})–ppy(π) character. The LUMOs of complex **12** are a degenerate couple of π* character delocalized on both the phenyl and pyridine moieties of the ppy ligands. At higher energies two almost degenerate

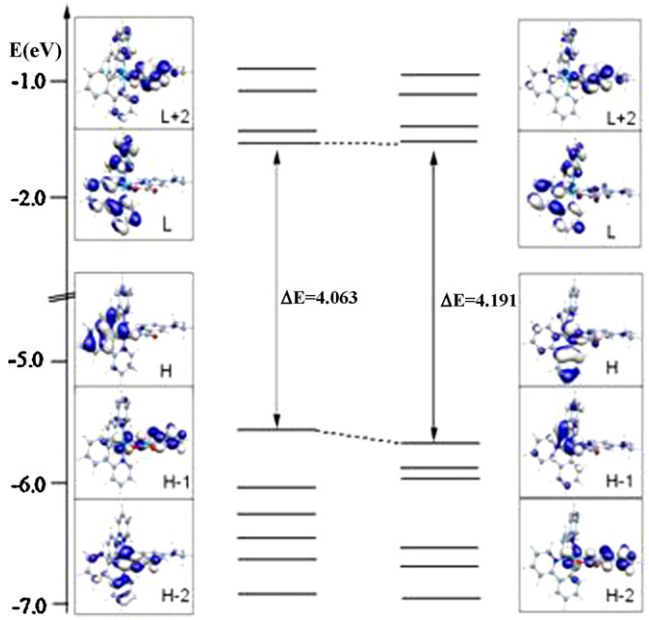

Fig. 19. Frontier molecular orbitals of N984 (**11**) (left) and N984b (**11b**) (right). Reproduced from Ref. [60] by permission of The Royal Society of Chemistry.

Table 3
Comparison between calculated lowest singlet-triplet transitions (eV) related emission and experimental high-energy emission features (eV) for complexes **12**–**15** in dichloromethane solution.

	12	13	14	15
Exp.	2.64	2.67	2.70	2.75
S_0–T_1	2.58	2.64	2.73	2.82

Source: Data from Ref. [57].

orbitals (LUMO+2/LUMO+3) of π* character, localized on the pyridine moieties of ppy, are found. The corresponding phenyl π* orbitals (LUMO+4/LUMO+5) are found still at higher energies. The molecular orbitals of complex **14** are qualitatively similar to those of complex **12**. For the dimethylamino-substituted complexes **13** and **15**, two orbitals showing sizable contributions from the dimethylamino N lone-pairs insert among the HOMOs. For all the investigated complexes the same LUMOs pattern is calculated, apart from the fact that complexes **13** and **15** show a small contribution from the dimethylamino N lone-pairs in the LUMO+2/LUMO+3.

The absorption spectra of the investigated complexes show similar features, with the low-energy spectroscopic region being dominated by transitions of main MLCT character, while at higher energy transitions of main π–π* character are found. Here we only briefly discuss the absorption spectrum of complex **12**. At its ground state geometry, the lowest TDDFT excited states of **12** are calculated to be of triplet character at 442 and 439 nm, essentially corresponding to HOMO–LUMO and HOMO–LUMO+1 MLCT transitions. The calculated and experimental emission maxima of the reported anionic complexes were in reasonable agreement, within 0.1 eV, even though for **12** and **13** the calculated results were red-shifted while for **14**–**15** a blue-shift was computed compared with experimental data, see Table 3.

3.4. Spin–orbit coupling and solvation effects

It is finally interesting to exploit our computational results to rationalize the general experimental trend of radiative rate constants [55b]. In the case of complexes **1**–**3,** k_r decreases with increasing emission energy, suggesting a sizable decrease in the oscillator strength of the emitting transition on going from **1** to **3**. Straightforward application of Einstein relation, would imply a decrease of the oscillator strength by 2.2 and 1.9 on going from **1** to **2** and from **2** to **3**, respectively.

We thus estimated the amount of metal character in the lowest singlet–triplet transitions by multiplying the squared coefficient of the TDDFT eigenvector characterizing the excited state by the percentage of metal character in the associated starting orbitals. By doing so and considering the T_1 optimized geometries, we calculate metal contributions to the lowest excited singlet–triplet excitations of 45, 19 and 10% for **1**, **2** and **3**, respectively. According to this approximate treatment, the increased π–π* character calculated for the lowest triplet excited state in **3** and **2** compared with **1** results in a diminished spin–orbit coupling for **2** and **3**, thus contributing to the observed reduction of k_r values. Recently, we re-investigated complexes **1**–**3** by means of quadratic response theory, thus including a more rigorous treatment of spin–orbit interactions on the TDDFT excitation energies [103]. The calculated phosphorescence lifetimes of **1**–**3** obtained by quadratic response theory agreed as order of magnitude with experimental values derived from photo-physical measurements but a reversed trend was retrieved in calculated phosphorescence lifetimes between theory and experiment.

Given the importance of solvation effects in determining the correct state assignment in the present compounds and in general in transition metals complexes, we decided to deeply investigate the effect of different solvents on the nature of the lowest excited states of complexes **2** and **3**, considering the optimized triplet geometries [58]. The most interesting variation observed with changing the solvent polarity is the huge change in the composition of the lowest excited triplet state. A strong contribution from the HOMO−2 → LUMO excitation arises with increasing the solvent polarity. For **2** such contribution is below 0.1 in vacuo reaching a 0.39 value in water. Thus the nature of the lowest triplet excited state, which we identify with the emitting state, changes dramatically as a function of the environment. The singlet–singlet manifold seemed to be affected to a lower extent by the environment. As a consequence of these changes, we expect significant variations in all the properties connected to the excited state nature, in particular to the spin–orbit coupling with the singlet manifold. Most notably, since the HOMO−2 → LUMO excitation introduces a sizable π–π* character into the lowest singlet–triplet transition, with a consequent decrease of metal character into the emitting excited state, a significant change in the transition probability for the triplet–singlet emission is to be expected by changing the solvent and in particular by considering results in vacuo or in solution. These considerations are probably responsible for the unbalanced evaluation of phosphorescence lifetimes along the **1**–**3** series obtained by quadratic response calculations in vacuo.

4. Ru(II) and Ir(III) complexes for NLO applications

Ru(II) and Ir(III) compounds have emerged as interesting molecular chromophores endowed with high and tunable second order nonlinear optical (NLO) properties. Compared with traditional organic NLO chromophores, transition metal compounds can provide additional electronic effects acting on the NLO response, which can be modulated by virtue of the nature, oxidation state and coordination sphere of the metal center [104]. Notably, coordination to a metal of second order push-pull NLO chromophores such as stilbazoles, bipyridine ligands, phenanthrolines and terpyridine ligands bearing a donor group produces a significant increase of their NLO response, due to a red-shift of the intraligand charge-transfer transition (ILCT) induced by the metal acting as a Lewis accep-

tor. On the contrary when the NLO chromophores bear a strong electron acceptor group, the NLO response is mainly controlled by metal to ligand charge-transfer transitions (MLCT) [104]. Ru(II) complexes with octupolar and dipolar NLO response have been deeply investigated [105–107]. In most cases, such investigations have been assisted by TDDFT and hyperpolarizability calculations to gain insight into the electronic transitions being at the origin of the NLO response in such systems. Ir(III) cyclometalated complexes have, on the other hand, only recently received attention as materials for NLO [42–44]. Most notably, these cyclometalated cationic Ir(III) complexes show relatively high energy absorptions, so that their high NLO response is reached without any cost in transparency, a crucial aspect in the design of NLO-phores.

Recently, the molecular second order nonlinear optical properties of the cationic $[Ir(ppy)_2(5\text{-}X\text{-}1,10\text{-}phen)][PF_6]$ (X = Me, NMe_2, NO_2) complexes were reported, indicating that cyclometalated Ir(III) complexes are characterized by one of the highest NLO response ever reported for a metal complex [42]. This response appears to be controlled by MLCT transitions from Ir(III) to the phenanthroline ligand, as confirmed by the TDDFT calculations reviewed below, so that the highest absolute $\mu\beta$ value, the vector product of the dipole moment μ times the hyperpolarizability tensor β, is obtained for the phenanthroline bearing the strong electron-withdrawing group NO_2. To provide detailed insight into factors governing the NLO properties of the investigated complexes, we performed DFT calculations on the complexes with X = NMe_2 and NO_2, **5** and **6**, respectively, these species being representative of strong electron-donating and electron-withdrawing phenanthroline substituents.

A comparison of the calculated absorption spectra for complexes **5** and **6** is reported in Fig. 20. The absorption spectra are dominated by MLCT and π–π^* excitations in the lower and upper energy spectroscopic regions, respectively. As it can be noticed, the agreement between theory and experiment is more than satisfactory. A distinctive feature of complex **5** is the presence of a low-lying (458 nm) and intense (f = 0.082) ILCT excitation originating from the NMe2-substituted phenanthroline ligand, which is missing in complex **6**.

Inspection of the calculated contributions to the hyperpolarizability tensor β for both complexes reveals that while for **6** β is exclusively the sum of negative contributions, for **5** counteracting positive and negative contributions to the NLO response are calculated. In agreement with the experimental evidence, this provides for **5** a β value which is about 5 times lower than the value found for **6**. For complex **5**, the largest positive contribution to the overall NLO response is originated from the ILCT transition discussed above, while MLCT excitations to the phenanthroline ligand provide here a negative response. The different sign of the MLCT and ILCT contributions stems from the different variation of the excited state dipole moment of the two types of transitions. Although MLCT excitations to the cyclometalating ligands provide significantly intense contributions to the absorption spectra of both compounds, these excitations do not significantly contribute to the NLO response because of a small variation of excited state dipole moment compared with the ground state one.

A subsequent combined experimental (EFISH and ^1H and ^{19}F PGSE NMR) and theoretical (DFT, TDDFT, sum over state, SOS) investigation on the same compounds indicated that ion pairing, controlled by the nature of the counterion and by the concentration, may significantly affect the $\mu\beta$ values of these cationic NLO chromophores. In CH_2Cl_2, concentration-dependent high absolute values of $\mu\beta$ are obtained for $[Ir(ppy)_2(5\text{-}NO_2\text{-}1,10\text{-}phen)Y$ when Y is a weakly interacting anion such as PF_6^-, whereas with a counterion such as $C_{12}H_{25}SO_3^-$ or I^-, which form tight ion-pairs, the absolute value of $\mu\beta$, is lower and quite independent from concentration [43].

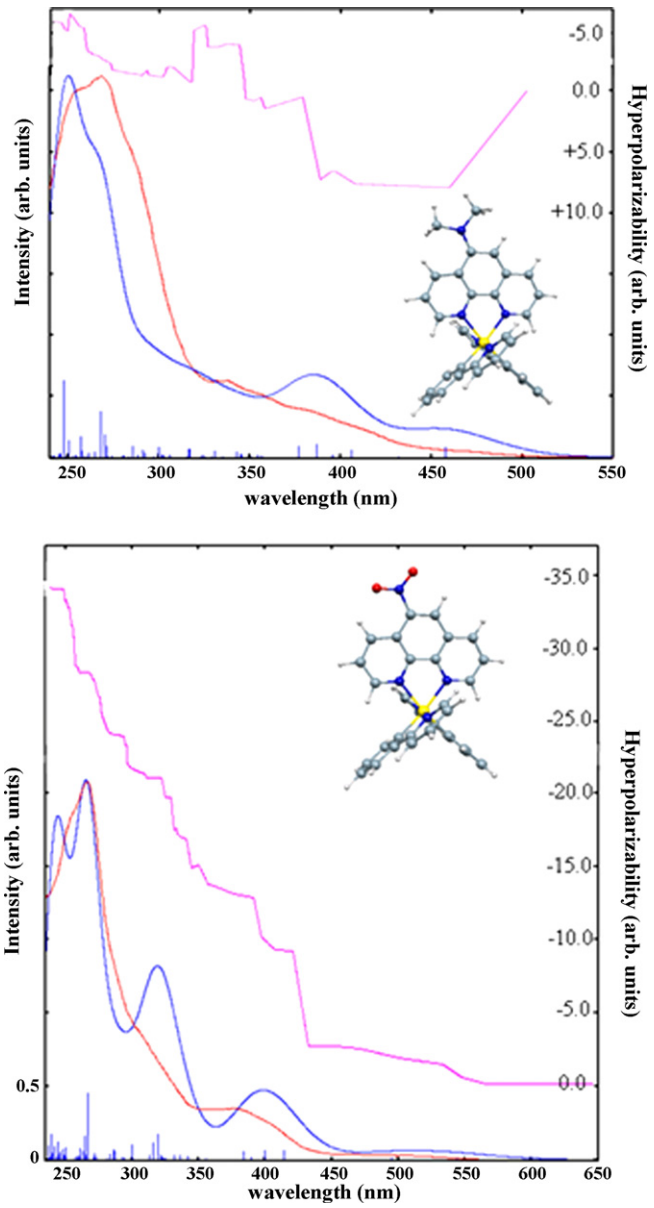

Fig. 20. Experimental (red) and calculated (blue) absorption spectra and calculated contributions to the quadratic hyperpolarizability (magenta) along with molecular structures for the **5** (upper panel) and **6** sum over state, (lower panel) complexes. Reproduced from Ref. [42a] by permission of The Royal Society of Chemistry.

To provide insight into the effect of ion pairing on the structural, electronic and second order NLO properties of the cationic Ir(III) NLO chromophores investigated in this work, we performed DFT and TDDFT comparative calculations on both the cationic complex **6** and its ion-pair with PF_6^-, taking into account solvation effects [43]. Several different mutual arrangements of the cation and anion in the ion-pair structure were investigated, followed by full geometry optimization. A minimum energy for the structure of the ion-pair was found with the PF_6^- anion localized above the plane of the phenanthroline ligand, consistent with the arrangement found by means of ^{19}F,^1H-HOESY NMR spectroscopy.

The optimized molecular structure of the Ir(III) complex is only slightly affected by the formation of the ion-pair, the most noticeable effect being a slight distortion from the planar geometry of the 5-NO_2-1,10-phenanthroline ligand. The comparison between the frontier molecular orbitals of the cation and its ion-pair with PF_6^- are reported in Fig. 21, together with isodensity plots of selected

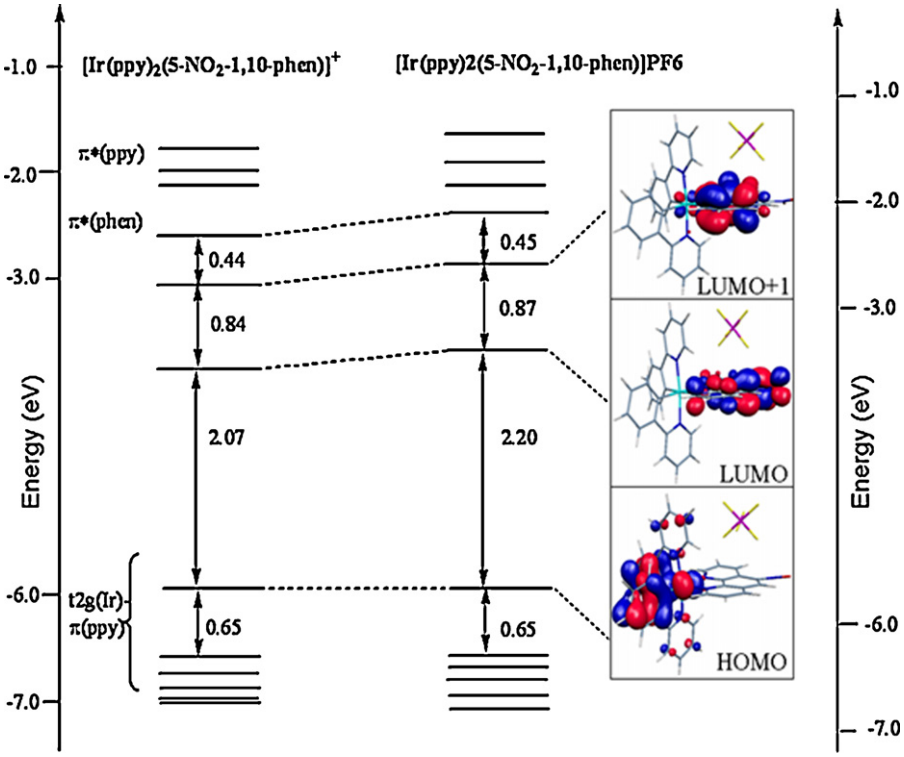

Fig. 21. Energy and character of the frontier molecular orbitals of $[Ir(ppy)_2(5\text{-}NO_2\text{-}1,10\text{-}phen)]^+$ and of $[Ir(ppy)_2(5\text{-}NO_2\text{-}1,10\text{-}phen)]PF_6$. The energy scales have been aligned so that the energy of the HOMO may coincide (notice the different scale on the left and right panels).
Reproduced with permission from Ref. [43]. Copyright Wiley-VCH Verlag GmbH & Co. KGaA.

molecular orbitals for the latter. The basic electronic structure of the cation is maintained also for the ion-pair, since the PF_6^- counterion does not affect the overall character of the frontier molecular orbitals, while some significant differences are found on the energy levels. In particular, aligning the HOMO energies to the same value, ion pairing produces a destabilization of the LUMOs set relative to the HOMOs, due to the perturbation exerted by PF_6^- on the π^* orbitals of the phenanthroline ligand. On overall, the HOMO–LUMO gap increases, passing from 2.07 eV for the cation to 2.20 eV for the ion-pair with PF_6^- (Fig. 21). Besides, calculations show that while in the cation the dipole moment is roughly aligned along the metal-phenanthroline axis, the presence of the PF_6^- counterion introduces a significant component along the direction connecting the PF_6^- anion and the Ir(III) center.

The computed absorption spectra for the cation **6** and the ion-pair are quite similar although showing appreciable variations in the position and intensity of the low energy bands related to HOMO–LUMO transitions at about 330–400 nm, in line with the perturbation exerted by the PF_6^- anion on the LUMO levels. The SOS investigation of the second order NLO response performed for the ion-pair revealed that, also in the ion-pair the charge transfer transitions from the $Ir(t_{2g})$–ppy(π) HOMO to the π^* LUMO and LUMO+1 levels of the phenanthroline ligand, are still those mainly affecting the value of the EFISH β. Most notably, a decrease of the absolute value of the EFISH molecular β was calculated by shifting from the cation to its ion-pair, although maintaining the same sign. Such a decrease, is clearly related to the opening of the HOMO–LUMO gap, which produces MLCT excitations of higher energy, which in turn should lead to a reduced second order NLO response, as expected on the basis of the two-level model. However, since the EFISH measurements give only the projection of the vectorial component β_{vec} along the dipole moment vector, from our theoretical investigation we can only suggest that ion pairing should produce a lowering of β. The effect on the value of the dipole moment is not so clear since it is difficult to define a precise dipole moment for cationic species.

Motivated by these results, a recent experimental EFISH investigation revealed that also the prototype $[Ir(ppy)_2(RCOCR'COR)]$ (R = Me; R′ = H) complex show an unexpected second order non linear optical response, as indicated by the EFISH technique, which was attributed by a SOS-TDDFT investigation mainly to intraligand charge transfer transitions involving the cyclometalated ligands. The lowest 40–60 singlet–singlet excitation energies, transition dipole moments, oscillator strengths and excited states dipole moments were calculated by TDDFT, allowing the simulation of the electronic absorption spectra up to ca. 250 nm and the qualitative characterization of the excited states mainly responsible of the static second-order NLO properties by means of an approximate SOS approach.

The calculated and experimental electronic spectra of the Ir(III) complex (Fig. 22) nicely agree, both in terms of absolute band positions and relative intensities, especially taking into consideration the rather limited dimensions of the basis set and the neglect of spin-orbit coupling in the excitation energies. In general, the low energy portion of the spectra, up to 300 nm, is dominated by MLCT transitions from the Ir-ppy based HOMOs to both the acac- and ppy-based LUMOs, while the higher energy part of the spectrum is dominated by more intense intraligand transitions of the ppy ligands, partially mixed with MLCT character.

The SOS contribution of each excited state to the static EFISH hyperpolarizability is reported in Fig. 22 as a function of the transition energy. Counteracting positive and negative contributions to the quadratic hyperpolarizability have been illustrated, the latter determining the negative sign of the converged value. The largest positive contributions to the quadratic hyperpolarizability are originated from transitions at 390 nm (3.18 eV) and 350 nm (3.55 eV), respectively, with dominating MLCT character (HOMO−1 → LUMO, Fig. 22). The strongest negative contributions are originated instead

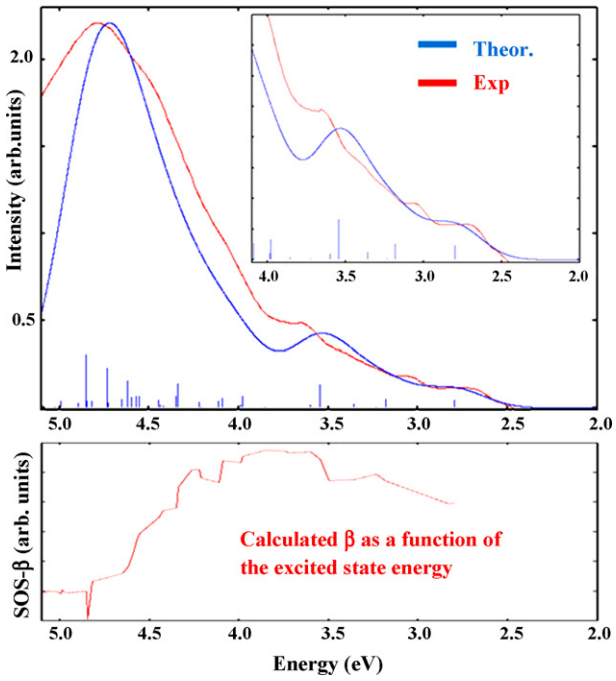

Fig. 22. Upper panel: Comparison between the calculated and experimental absorption spectra for [Ir(ppy)$_2$(acac)]. Lower panel: Calculated contributions to the quadratic hyperpolarizability.
Redrawn from data from Ref. [44].

from a series of higher energy transitions involving mainly ppy-ILCT transitions, with a limited amount of metal character (for instance HOMO−5 → LUMO−1).

5. Conclusions

We have reviewed the main results obtained from the application of quantum chemical methods to the study of the electronic, optical and non-linear optical properties of Ru(II)- and Ir(III)-polypiridyl complexes mostly employed in DSC, OLED and NLO devices.

The advent of methods rooted into density functional theory (DFT) has profoundly revolutionized the field of computer simulations of complex systems, and most of current theoretical investigations are performed within the DFT framework. Substantial theoretical and computational advances in the treatment of excited states by time dependent DFT, solute–solvent interactions by continuum solvation models and ab initio molecular dynamics, allow nowadays researchers to perform accurate simulations of relatively large systems under realistic conditions, including a thorough characterization of the systems excited states.

Thanks to these efforts, time dependent DFT calculations on transition metal complexes are nowadays performed in many experimental laboratories to assist the design of new compounds and rationalize experimental trends. As a consequence, based on a careful computational set up, it is now possible to scrutinize new compounds with target characteristics even before their synthesis. This is particularly relevant to the three explored fields of application of this review, whereby prediction of the energy levels and their character, of optical absorption and emission spectra and of hyperpolarizabilities can help us to focus exclusively on the most promising compounds, thus allowing for considerable savings of human and financial resources.

The simulation of hybrid molecular/semiconductor heterointerfaces by DFT is also possible and recently it has reached the same level of accuracy and realism as that typical of the investigation of isolated metal complexes. By quantitative reproduction of relevant experimental information for extended models under realistic conditions it has been indeed possible to understand in deeper details some of the fundamental factors affecting the DSCs functioning and therefore efficiency. This information is now being processed for the design of new and more efficient sensitizers and materials. We thus foresee an increasing role of modeling in the rapid exploitation of hybrid/organic materials for photonic applications.

Despite all these advances, yet “the simulation” of the microscopic functioning of a device is still to come, due to inherent difficulties in accurately describing at the same time all the fundamental ingredients and processes underlying the functioning of such complex systems. We believe that the key to success in this field is definitely represented by a multi-technique computational approach which integrates different codes and techniques bridging quantum chemistry, materials science and solid-state physics.

We would finally like to mention the relevant role of the interplay between theory and experiments. While theoretical and computational advances constitute the basis for successful simulation of complex systems, it is only by the continuous exchange of ideas and information between theory and experiment that we expect substantial impulse and new ideas able to revolutionize the field of hybrid/organic materials for photonic applications.

Acknowledgments

We thank Fondazione Istituto Italiano di Tecnologia (IIT), Project SEED 2009 (HELYOS), and MIUR-PRIN 2008 for financial support.

References

[1] B. O'Regan, M. Grätzel, Nature 353 (1991) 737.
[2] J.M. Rehm, G.L. McLendon, Y. Nagasawa, K. Yoshihara, J. Moser, M. Grätzel, J. Phys. Chem. B 100 (1996) 9577.
[3] A. Hagfeldt, M. Grätzel, Chem. Rev. 95 (1995) 49.
[4] M. Grätzel, Nature 414 (2001) 338.
[5] M.K. Nazeeruddin, Q. Wang, L. Cevey, V. Aranyos, P. Liska, E. Figgemeier, C. Klein, N. Hirata, S. Koops, S.A. Haque, J.R. Durrant, A. Hagfeldt, A.B.P. Lever, M. Grätzel, Inorg. Chem. 45 (2006) 787.
[6] P.V. Kamat, J. Phys. Chem. C 111 (2007) 2834.
[7] C. Adachi, M.A. Baldo, M.E. Thompson, S.R. Forrest, J. Appl. Phys. 90 (2001) 5048.
[8] M.A. Baldo, S. Lamansky, P.E. Burrows, M.E. Thompson, S.R. Forrest, Appl. Phys. Lett. 75 (1999) 4.
[9] M. Ikai, S. Tokito, Y. Sakamoto, T. Suzuki, Y. Taga, Appl. Phys. Lett. 79 (2001) 156.
[10] M.K. Nazeeruddin, R. Humphry-Baker, D. Berner, B.S. Rivier, L. Zuppiroli, M. Grätzel, J. Am. Chem. Soc. 125 (2003) 8790.
[11] J. Zyss, Molecular Nonlinear Optics: Materials, Physics and Devices, Academic Press, Boston, 1994.
[12] A.D. Becke, Chem. Phys. 98 (1993) 5648.
[13] G. te Velde, F.M. Bickelhaupt, E.J. Baerends, S.J.A. van Gisbergen, C. Fonseca-Guerra, J.G. Snjders, T. Ziegler, J. Comput. Chem. 22 (2001) 931.
[14] M.J. Frisch, G.W. Trucks, H.B. Schlegel, G.E. Scuseria, M.A. Robb, J.R. Cheeseman, J.A. Montgomery Jr., T. Vreven, K.N. Kudin, J.C. Burant, J.M. Millam, S.S. Iyengar, J. Tomasi, V. Barone, B. Mennucci, M. Cossi, G. Scalmani, N. Rega, G.A. Petersson, H. Nakatsuji, M. Hada, M. Ehara, K. Toyota, R. Fukuda, J. Hasegawa, M. Ishida, T. Nakajima, Y. Honda, O. Kitao, H. Nakai, M. Klene, X. Li, J.E. Knox, H.P. Hratchian, J.B. Cross, C. Adamo, J. Jaramillo, R. Gomperts, R.E. Stratmann, O. Yazyev, A.J. Austin, R. Cammi, C. Pomelli, J.W. Ochterski, P.Y. Ayala, K. Morokuma, G.A. Voth, P. Salvador, J.J. Dannenberg, V.G. Zakrzewski, S. Dapprich, A.D. Daniels, M.C. Strain, O. Farkas, D.K. Malick, A.D. Rabuck, K. Raghavachari, J.B. Foresman, J.V. Ortiz, Q. Cui, A.G. Baboul, S. Clifford, J. Cioslowski, B.B. Stefanov, G. Liu, A. Liashenko, P. Piskorz, I. Komaromi, R.L. Martin, D.J. Fox, T. Keith, M.A. Al-Laham, C.Y. Peng, A. Nanayakkara, M. Challacombe, P.M.W. Gill, B. Johnson, W. Chen, M.W. Wong, C. Gonzalez, J.A. Pople, Gaussian 03, Revision B.05, Gaussian, Inc., Pittsburgh, PA, 2003.
[15] http://www.kjemi.unio.no/software/dalton/dalton.html.
[16] M. Häser, R. Ahlrichs, J. Comput. Chem. 10 (1989) 104.
[17] http://www.quantum-espresso.org.
[18] G. Kresse, J. Hafner, Phys. Rev. B 49 (1994) 14251.
[19] V.R. Saunders, R. Dovesi, C. Roetti, R. Orlando, C.M. Zicovich-Wilson, N.M. Harrison, K. Doll, B. Civalleri, I. Bush, Ph. D'Arco, M. Llunell, Crystal 03 User's Manual, Università di Torino, Torino, Italy, 2003.
[20] R. Car, M. Parrinello, Phys. Rev. Lett. 55 (1985) 2471.
[21] P. Giannozzi, F. De Angelis, R. Car, J. Chem. Phys. 120 (2004) 5903.

[22] F. De Angelis, S. Fantacci, A. Sgamellotti, Coord. Chem. Rev. 205 (2006) 1497.
[23] M. Pavone, P. Cimino, F. De Angelis, V. Barone, J. Am. Chem. Soc. 128 (2006) 4338.
[24] B. Hetényi, F. De Angelis, P. Giannozzi, R. Car, J. Phys. Chem. 120 (2004) 8632.
[25] S. Fantacci, F. De Angelis, A. Sgamellotti, A. Marrone, N. Re, J. Am. Chem. Soc. 127 (2005) 14144.
[26] F. De Angelis, A. Jarzecki, R. Car, T.G. Spiro, J. Phys. Chem. B 109 (2005) 3065.
[27] S. Fantacci, F. De Angelis, A. Selloni, J. Am. Chem. Soc. 125 (2003) 4381.
[28] O. Crescenzi, M. Pavone, F. De Angelis, V. Barone, J. Phys. Chem. B 109 (2005) 445.
[29] S. Miertus, E. Scrocco, J. Tomasi, Chem. Phys. 55 (1981) 117.
[30] A. Klamt, G. Schurmann, J. Chem. Soc. Perkin Trans. 2 (1993) 799.
[31] M. Cossi, N. Rega, G. Scalmani, V. Barone, J. Comp. Chem. 24 (2003) 669.
[32] A. Klamt, V. Jonas, J. Chem. Phys. 105 (2006) 9972.
[33] M. Casida, Time dependent density functional response theory for molecules, in: D.P. Chong (Ed.), Recent Advances in Density Functional Methods, vol. 1, World Scientific, Singapore, 1995, p. 155.
[34] S. Fantacci, A. Migani, M. Olivucci, J. Phys. Chem. A 108 (2004) 1208.
[35] A. Dreuw, M. Head-Gordon, J. Am. Chem. Soc. 126 (2004) 4007.
[36] For a review, see: A. Vlcek, S. Zalis, Coord. Chem. Rev. 251 (2007) 258.
[37] M. Cossi, V. Barone, J. Chem. Phys. 115 (2001) 4717.
[38] F. Furche, A. Ahlrichs, J. Chem. Phys. 117 (2002) 7433.
[39] B. Walker, A.M. Saitta, R. Gebauer, S. Baroni, Phys. Rev. Lett. 96 (2006) 113001.
[40] (a) M. Häser, R. Ahlrichs, J. Comput. Chem. 10 (1989) 104;
(b) R. Ahlrichs, M. Bär, M. Häser, H. Horn, C. Kölmel, J. Comput. Chem. 162 (1989) 165;
(c) H. Weiss, R. Ahlrichs, M. Häser, J. Chem. Phys. 99 (1993) 1262;
(d) R. Bauernschmitt, R. Ahlrichs, Chem. Phys. Lett. 256 (1996) 454;
(e) R. Bauernschmitt, R. Ahlrichs, Chem. Phys. Lett. 104 (1996) 9047;
(f) F. Furche, R. Ahlrichs, J. Chem. Phys. 117 (2004) 7433.
[41] L. Storchi, L. Belpassi, F. Tarantelli, A. Sgamellotti, H.M. Quiney, J. Chem. Theory Comp. 6 (2010) 384.
[42] (a) C. Dragonetti, S. Righetto, D. Roberto, R. Ugo, A. Valore, S. Fantacci, A. Sgamellotti, F. De Angelis, Chem. Commun. (2007) 4116;
(b) C. Dragonetti, S. Righetto, D. Roberto, R. Ugo, A. Valore, F. De Martin, F. De Angelis, A. Sgamellotti, S. Fantacci, Inorg. Chim. Acta 361 (2008) 4070;
(c) C. Dragonetti, S. Righetto, D. Roberto, A. Valore, T. Benincori, F. Sannicolò, S. Fantacci, F. De Angelis, J. Mater. Sci. Mater. Electron. 20 (2009) 460.
[43] A. Valore, E. Cariati, C. Dragonetti, S. Righetto, D. Roberto, R. Ugo, F. De Angelis, S. Fantacci, A. Sgamellotti, A. Macchioni, D. Zuccaccia, Chem. Eur. J. 16 (2010) 4814.
[44] A. Valore, A. Colombo, C. Dragonetti, S. Righetto, D. Roberto, R. Ugo, F. De Angelis, S. Fantacci, Chem. Commun. 46 (2010) 2414.
[45] M.K. Nazeeruddin, F. De Angelis, S. Fantacci, A. Selloni, G. Viscardi, P. Liska, S. Ito, B. Takeru, M. Grätzel, J. Am. Chem. Soc. 127 (2005) 16835.
[46] F. De Angelis, S. Fantacci, A. Selloni, Chem. Phys. Lett. 389 (2004) 204.
[47] F. De Angelis, S. Fantacci, A. Selloni, M.K. Nazeeruddin, Chem. Phys. Lett. 415 (2005) 115.
[48] C. Barolo, M.K. Nazeeruddin, S. Fantacci, D. Di Censo, P. Comte, P. Liska, G. Viscardi, P. Quagliotto, F. De Angelis, S. Ito, M. Grätzel, Inorg. Chem. 45 (2006) 4642.
[49] M.K. Nazeeruddin, T. Bessho, L. Cevey, S. Ito, C. Klein, F. De Angelis, S. Fantacci, P. Comte, P. Liska, H. Imai, M. Grätzel, J. Photochem. Photobiol. A 185 (2007) 331.
[50] A. Abbotto, C. Barolo, L. Bellotto, F. De Angelis, M. Grätzel, N. Manfredi, C. Marinzi, J.-H. Yum, M.K. Nazeeruddin, Chem. Commun. 42 (2008) 5318.
[51] A. Abbotto, F. Sauvage, C. Barolo, F. De Angelis, S. Fantacci, M. Graetzel, N. Manfredi, C. Marinzi, M.K. Nazeeruddin, Dalton Trans. 40 (2011) 234.
[52] S. Kim, J.K. Lee, S.O. Kang, J. Ko, J.-H. Yum, S. Fantacci, F. De Angelis, D. Di Censo, M.K. Nazeeruddin, M. Grätzel, J. Am. Chem. Soc. 128 (2006) 16701.
[53] J.-H. Yum, P. Walter, S. Huber, C. Rentsch, T. Geiger, F. Nüesch, F. De Angelis, M. Grätzel, M.K. Nazeeruddin, J. Am. Chem. Soc. 129 (2007) 10320.
[54] D.P. Hagberg, J.-H. Yum, H.J. Lee, F. De Angelis, T. Marinado, K.M. Karlsson, R. Humphry-Baker, L. Sun, A. Hagfeldt, M. Grätzel, M.K. Nazeeruddin, J. Am. Chem. Soc. 130 (2008) 6259.
[55] (a) M.K. Nazeeruddin, R.T. Wegh, Z. Zhou, C. Klein, A. Wang, F. De Angelis, S. Fantacci, M. Grätzel, Inorg. Chem. 45 (2006) 9254;
(b) F. De Angelis, S. Fantacci, N. Evans, C. Klein, S.M. Zakeeruddin, J.-E. Moser, K. Kalyanasundaram, H.J. Bolink, M. Grätzel, M.K. Nazeeruddin, Inorg. Chem. 46 (2007) 5989.
[56] C. Dragonetti, L. Falciola, P. Mussini, S. Righetto, D. Roberto, R. Ugo, A. Valore, F. De Angelis, S. Fantacci, A. Sgamellotti, M. Ramon, M. Muccini, Inorg. Chem. 46 (2007) 8533.
[57] D. Di censo, S. Fantacci, F. De Angelis, C. Klein, N. Evans, K. Kalyanasundaram, H.J. Bolink, M. Grätzel, M.K. Nazeeruddin, Inorg. Chem. 47 (2008) 980.
[58] F. De Angelis, L. Belpassi, S. Fantacci, J. Mol. Struct. (THEOCHEM) 904 (2009) 74.
[59] H.J. Bolink, F. De Angelis, E. Baranoff, C. Klein, S. Fantacci, E. Coronado, M. Sessolo, K. Kalyanasundaram, M. Grätzel, Md.K. Nazeeruddin, Chem. Commun. (2009) 4672.
[60] E. Baranoff, H.J. Bolink, F. De Angelis, S. Fantacci, D. Di Censo, K. Djellab, M. Grätzel, M.K. Nazeeruddin, Dalton Trans. 39 (2010) 8914.
[61] M.K. Nazeeruddin, M. Grätzel, in: V. Ramamurthy, K.S. Schanze (Eds.), Molecular and Supramolecular Photochemistry, vol. 10, Marcel Dekker, New York, 2003, p. 301.
[62] M. Grätzel, Inorg. Chem. 44 (2005) 6841.
[63] M.K. Nazeeruddin, A. Kay, I. Rodicio, R. Humphry-Baker, E. Muller, P. Liska, N. Vlachopoulos, M. Grätzel, J. Am. Chem. Soc. 115 (1993) 6382.
[64] T. Horiuchi, H. Miura, K. Sumioka, S. Uchida, J. Am. Chem. Soc. 126 (2004) 12218.
[65] C. Daul, E.J. Baerends, P. Vernooijs, Inorg. Chem. 33 (1994) 3538.
[66] J.-P. Sauvage, J.-P. Collin, J.-C. Chambron, S. Guillerez, C. Coudret, V. Balzani, F. Barigelletti, L. De Cola, L. Flamigni, Chem. Rev. 94 (1994) 993.
[67] H. Rensmo, S. Södergren, L. Patthey, K. Westmark, L. Vayssieres, O. Khole, P.A. Brühwiler, A. Hagfeldt, H. Siegbahn, Chem. Phys. Lett. 274 (1997) 51.
[68] F. Cecchet, A.M. Gioacchini, M. Marcaccio, F. Paolucci, S. Roffia, M. Alebbi, C. Alberto Bignozzi, J. Phys. Chem. B 106 (2002) 3926.
[69] Md.K. Nazeeruddin, S.M. Zakeeruddin, R. Humpry-Baker, S.I. Gorelsky, A.B.P. Lever, M. Grätzel, Coord. Chem. Rev. 208 (2000) 213.
[70] J.E. Monat, J.H. Rodriguez, J.K. McCusker, J. Phys. Chem. A 106 (2002) 7399.
[71] J.-F. Guillemoles, V. Barone, L. Joubert, C. Adamo, J. Phys. Chem. A 106 (2002) 11354.
[72] E.M.J. Johansson, M. Hedlund, H. Siegbah, H. Rensmo, J. Phys. Chem. B 109 (2005) 22256.
[73] Md.K. Nazeeruddin, S.M. Zakeeruddin, R. Humphry-Baker, M. Jirousek, P. Liska, N. Vlachopoulos, V. Shklover, C.H. Fischer, M. Grätzel, Inorg. Chem. 38 (1999) 6298.
[74] F. De Angelis, S. Fantacci, A. Selloni, Nanotechnology 19 (2008) 424002.
[75] K. Kalyanasundaram, M. Grätzel, Coord. Chem. Rev. 177 (1998) 347.
[76] G. Wolfbauer, A.M. Bond, G.B. Deacon, D.R. MacFarlane, L. Spiccia, J. Am. Chem. Soc. 122 (2000) 130.
[77] (a) Md.K. Nazeeruddin, S.M. Zakeeruddin, J.-J. Lagref, C. Barolo, G. Viscardi, P. Liska, P. Comte, K. Schenk, M. Grätzel, Coord. Chem. Rev. 248 (2004) 1317;
(b) S.M. Zakeeruddin, Md.K. Nazeeruddin, R. Humphry-Baker, P. Pechy, P. Quagliotto, C. Barolo, G. Viscardi, M. Grätzel, Langmuir 18 (2002) 952.
[78] Md.K. Nazeeruddin, Q. Wang, L. Cevey, V. Aranyos, P. Liska, E. Figgemeier, C. Klein, N. Hirata, S. Koops, S.A. Haque, J. Durrant, A. Hagfeldt, A.B.P. Lever, M. Grätzel, Inorg. Chem. 45 (2006) 787.
[79] (a) F. Gao, Y. Wang, J. Zhang, D. Shi, M. Wang, R. Humphry-Baker, P. Wang, S.-M. Zakeeruddin, M. Grätzel, Chem. Commun. (2008) 2635;
(b) F. Gao, Y. Wang, D. Shi, J. Zhang, M. Wang, X. Jing, R. Humphry-Baker, P. Wang, S.-M. Zakeeruddin, M. Grätzel, J. Am. Chem. Soc. 130 (2008) 10720.
[80] (a) C.-Y. Chen, S.-J. Wu, C.-G. Wu, J.-G. Chen, K.-C. Ho, Angew. Chem. Int. Ed. 45 (2006) 5822;
(b) C.-Y. Chen, S.-J. Wu, C.-G. Wu, J.-G. Chen, K.-C. Ho, Adv. Mater. 19 (2007) 3888;
(c) C.-Y. Chen, S.-J. Wu, C.-G. Wu, J.-G. Chen, K.-C. Ho, Adv. Funct. Mater. 17 (2007) 29.
[81] C.-Y. Chen, S.-J. Wu, J.-Y. Li, C.-G. Wu, J.-G. Chen, K.-C. Ho, Adv. Mater. 19 (2007) 3888.
[82] Y. Liu, A. Hagfeldt, X.R. Xiao, S.E. Lindquist, Sol. Energy Mater. Sol. Cells 55 (1998) 267.
[83] T. Bessho, T. Yoneda, E. Yum, J.-H. Guglielmi, M. Tavernelli, I. Imai, H. Rothlisberger, U. Nazeeruddin, Md.K.M. Grätzel, J. Am. Chem. Soc. 131 (2009) 5930.
[84] B.D. Koivisto, K.C.D. Robson, C.P. Berlinguette, Inorg. Chem. 48 (2009) 9644.
[85] F. De Angelis, A. Tilocca, A. Selloni, J. Am. Chem. Soc. 126 (2004) 15024.
[86] (a) P. Persson, M. Lundqvist, J. Phys. Chem. B 109 (2005) 11918;
(b) J. Schnadt, P.A. Bruhwiler, L. Patthey, J. O'Shea, M. Odelius, R. Ahuja, O. Karis, M. Bässler, P. Persson, H. Siegbahn, S. Lunell, N. Mårtensson, Nature 418 (2002) 620.
[87] M.J. Lundqvist, M. Nilsing, S. Lunell, B. Kermark, P. Persson, J. Phys. Chem. B 110 (2006) 20513.
[88] F. De Angelis, S. Fantacci, A. Selloni, Md.K. Nazeeruddin, M. Grätzel, J. Am. Chem. Soc. 129 (2007) 14156.
[89] M.K. Nazeeruddin, R. Humphry-Baker, P. Liska, M. Grätzel, J. Phys. Chem. B 107 (2003) 8981.
[90] F. De Angelis, S. Fantacci, A. Selloni, M. Grätzel, M.K. Nazeeruddin, Nano Lett. 7 (2007) 3189.
[91] P. Chen, J.-H. Yum, F. De Angelis, E. Mosconi, S. Fantacci, J.-J. Moon, R. Humphry Baker, J. Ko, Md.K. Nazeeruddin, M. Grätzel, Nano Lett. 9 (2009) 2487.
[92] F. De Angelis, S. Fantacci, A. Selloni, M.K. Nazeeruddin, M. Grätzel, J. Phys. Chem. C 114 (2010) 6054.
[93] F. Schiffmann, J. VandeVondele, J. Hutter, R. Wirz, A. Urakawa, A. Baiekr, J. Phys. Chem. C 114 (2010) 8398.
[94] Y. Ohsawa, S. Sprouse, K.A. King, M.K. DeArmond, K.W. Hanck, R.J. Watts, J. Phys. Chem. 91 (1987) 1047.
[95] F.O. Garces, K.A. King, R.J. Watts, Inorg. Chem. 27 (1988) 3464.
[96] A. King, R.J. Watts, J. Am. Chem. Soc 109 (1987) 1589.
[97] J.D. Slinker, A.A. Gorodetsky, M.S. Lowry, J. Wang, S. Parker, R. Rohl, S. Bernhard, S.G.G. Malliaras, J. Am. Chem. Soc. 126 (2004) 2763.
[98] F. Neve, M. La Deda, A. Crespini, A. Bellusci, F. Puntoriero, S. Campagna, Organometallics 23 (2004) 5856.
[99] (a) F. Santoro, R. Improta, A. Lami, J. Bloino, V. Barone, J. Chem. Phys. 126 (2007) 084509;
(b) F. Santoro, R. Improta, A. Lami, J. Bloino, V. Barone, J. Chem. Phys. 126 (2007) 169903;
(c) F. Santoro, R. Improta, A. Lami, J. Bloino, V. Barone, J. Chem. Phys. 126 (2007) 224311;
(d) F. Santoro, R. Improta, A. Lami, V. Barone, J. Chem. Phys. 126 (2007) 184102;
(e) F. Santoro, FCclasses code: visit http://village.unina.it.
[100] F. De Angelis, F. Santoro, K. Md, V. Nazeeruddin, Barone, J. Phys. Chem. B 112 (2008) 13181.

[101] S. Lamansky, P. Djurovich, D. Murphy, F. Abdel-Razzaq, R. Kwong, I. Tsyba, M. Bortz, B. Mui, R. Bau, M.E. Thompson, Inorg. Chem. 40 (2001) 1704.
[102] E. Baranoff, S. Fantacci, F. De Angelis, X. Zhang, R. Scopelliti, M. Graetzel, Md.K. Nazeeruddin, Inorg. Chem. 50 (2011) 451.
[103] B. Minaev, H. Ågren, F. De Angelis, Chem. Phys. 358 (2009) 245.
[104] For example see;
(a) D.R. Kanis, P.G. Lacroix, M.A. Ratner, T.J. Marks, J. Am. Chem. Soc. 116 (1994) 10089;
(b) J. Heck, S. Dabek, T. Meyer-Friedrichsen, H. Wong, Coord. Chem. Rev. 192 (1999) 1217;
(c) H. Le Bozec, T. Renouard, Eur. J. Inorg. Chem. (2000) 229;
(d) P.G. Lacroix, Eur. J. Inorg. Chem. (2001) 339;
(e) S. Di Bella, Chem. Soc. Rev. 30 (2001) 355;
(f) B.J. Coe, in: J.A. McCleverty, T.J. Meyer (Eds.), Comprehensive Coordination Chemistry II, vol. 9, Elsevier Pergamon, Oxford, UK, 2004, p. 621;
(g) B.J. Coe, N.R.M. Curati, Comments Inorg. Chem. 25 (2004) 147;
(h) E. Cariati, M. Pizzotti, D. Roberto, F. Tessore, R. Ugo, Coord. Chem. Rev. 250 (2006) 1210;
(i) B.J. Coe, Acc. Chem. Res. 39 (2006) 383;
(j) M.G. Humphrey, M. Samoc, Adv. Organomet. Chem. 55 (2008) 61.
[105] (a) F. Dumur, C.R. Mayer, K. Hoang-Thi, I. Ledoux-Rak, F. Miomandre, G. Clavier, E. Dumas, R. Méallet-Renault, M. Frigoli, J. Zyss, F. Sécheresse, Inorg. Chem. 48 (2009) 8120;
(b) T. Le Boulder, O. Maury, A. Bondon, K. Costuas, E. Amouyal, I. Ledoux, J. Zyss, H. Le Bozec, J. Am. Chem. Soc. 125 (2003) 12284.
[106] (a) B.J. Coe, J.H. Harris, B.S. Brunschwing, I. Asselberghs, K. Clays, J. Garín, J. Orduna, J. Am. Chem. Soc. 127 (2005) 13399;
(b) B.J. Coe, J.H. Harris, L.A. Jones, B.S. Brunschwing, K. Song, K. Clays, J. Garín, J. Orduna, S.J. Coles, M.B. Hursthouse, J. Am. Chem. Soc. 127 (2005) 4845;
(c) B.J. Coe, S.P. Foxon, E.C. Harper, M. Helliwell, J. Raftery, C.A. Swanson, B.S. Brunschwing, K. Clays, E. Franz, J. Garín, J. Orduna, P.N. Horton, M.B. Hursthouse, J. Am. Chem. Soc. 132 (2010) 1706.
[107] (a) L. Boubekeur-Lecaque, B.J. Coe, K. Clays, S. Foerier, T. Verbiest, I. Asselberghs, J. Am. Chem. Soc. 130 (2008) 3286;
(b) B.J. Coe, L.A. Jones, J.A. Harris, B.S. Brunschwing, I. Asselberghs, K. Clays, A. Persoons, J. Garín, J. Orduna, J. Am. Chem. Soc. 126 (2004) 3880;
(c) B.J. Coe, J.A. Harris, B.S. Brunschwing, J. Garín, J. Orduna, S.J. Coles, M.B. Hursthouse, J. Am. Chem. Soc. 126 (2004) 10418;
(d) B.J. Coe, L.A. Jones, J.A. Harris, B.S. Brunschwing, I. Asselberghs, K. Clays, A. Persoons, J. Am. Chem. Soc. 125 (2003) 862.